CANDIDATE WATER VAPOR LINES TO LOCATE THE H_2O SNOWLINE THROUGH HIGH-DISPERSION SPECTROSCOPIC OBSERVATIONS. I. THE CASE OF A T TAURI STAR

SHOTA NOTSU[1,7], HIDEKO NOMURA[2], DAIKI ISHIMOTO[1,2], CATHERINE WALSH[3], MITSUHIKO HONDA[4],
TOMOYA HIROTA[5], AND T. J. MILLAR[6]

[1] Department of Astronomy, Graduate School of Science, Kyoto University, Kitashirakawa-Oiwake-cho, Sakyo-ku, Kyoto 606-8502, Japan;
snotsu@kusastro.kyoto-u.ac.jp
[2] Department of Earth and Planetary Science, Tokyo Institute of Technology, 2-12-1 Ookayama, Meguro-ku, Tokyo 152-8551, Japan
[3] Leiden Observatory, Leiden University, P.O. Box 9513, 2300 RA Leiden, The Netherlands
[4] Department of Physics, School of Medicine, Kurume University, 67 Asahi-machi, Kurume, Fukuoka 830-0011, Japan
[5] National Astronomical Observatory of Japan, 2-21-1 Osawa, Mitaka, Tokyo 181-8588, Japan
[6] Astrophysics Research Centre, School of Mathematics and Physics, Queen's University Belfast, University Road, Belfast, BT7 1NN, UK
Received 2015 December 30; revised 2016 June 15; accepted 2016 June 16; published 2016 August 12

ABSTRACT

Inside the H_2O snowline of protoplanetary disks, water evaporates from the dust-grain surface into the gas phase, whereas it is frozen out onto the dust in the cold region beyond the snowline. H_2O ice enhances the solid material in the cold outer part of a disk, which promotes the formation of gas-giant planet cores. We can regard the H_2O snowline as the surface that divides the regions between rocky and gaseous giant planet formation. Thus observationally measuring the location of the H_2O snowline is crucial for understanding the planetesimal and planet formation processes, and the origin of water on Earth. In this paper, we find candidate water lines to locate the H_2O snowline through future high-dispersion spectroscopic observations. First, we calculate the chemical composition of the disk and investigate the abundance distributions of H_2O gas and ice, and the position of the H_2O snowline. We confirm that the abundance of H_2O gas is high not only in the hot midplane region inside the H_2O snowline but also in the hot surface layer of the outer disk. Second, we calculate the H_2O line profiles and identify those H_2O lines that are promising for locating the H_2O snowline: the identified lines are those that have small Einstein A coefficients and high upper state energies. The wavelengths of the candidate H_2O lines range from mid-infrared to sub-millimeter, and they overlap with the regions accessible to the Atacama Large Millimeter/sub-millimeter Array and future mid-infrared high-dispersion spectrographs (e.g., TMT/MICHI, SPICA).

Key words: astrochemistry – infrared: planetary systems – ISM: molecules – protoplanetary disks – stars: formation – submillimeter: planetary systems

1. INTRODUCTION

Protoplanetary disks are rotating accretion disks surrounding young newly formed stars (e.g., T Tauri stars, Herbig Ae/Be stars). They are composed of dust grains and gas, and contain all the material that will form planetary systems orbiting main-sequence stars (e.g., Armitage 2011). They are active environments for the creation of simple and complex molecules, including organic matter and H_2O (e.g., Caselli & Ceccarelli 2012; Henning & Semenov 2013; Pontoppidan et al. 2014). The physical and chemical environments of proto-planetary disks determine the properties of various planets, including mass and chemical composition (e.g., Öberg et al. 2011; Pontoppidan et al. 2014). Among all of the molecules in disks, H_2O is one of the most important in determining physical and chemical properties.

H_2O gas and ice likely carries most of the oxygen that is available, the only competitors are CO and possibly CO_2 (Pontoppidan & Blevins 2014; Walsh et al. 2015). In the hot inner regions of protoplanetary disks, H_2O ice evaporates from the dust-grain surfaces into the gas phase. On the other hand, it is frozen out on the dust-grain surfaces in the cold outer parts of the disk. The H_2O snowline is the surface that divides the disk into these two different regions (Hayashi 1981). H_2O ice enhances the solid material in the cold region beyond the H_2O snowline, and H_2O ice mantles on dust grains beyond the H_2O

snowline allow dust grains to stick at higher collisional velocities and promote efficient coagulation compared with collisions of refractory grains (e.g., Wada et al. 2013). As a result, the formation of the cores of gaseous planets are promoted in such regions. In the disk midplane, we can thus regard the H_2O snowline as the line that divides the regions of rocky planet and gas-giant planet formation (e.g., Hayashi 1981; Hayashi et al. 1985; Öberg et al. 2011). In the upper layers of the disk, the surface separating water vapor from water ice is determined by the photodesorption of water ice by the stellar UV radiation field in competition with freezeout of water onto dust grains (e.g., Blevins et al. 2016, see also Section 3.1).

Icy planetesimals, comets, and/or icy pebbles coming from outside the H_2O snowline may bring water to rocky planets including the Earth (e.g., Morbidelli et al. 2000, 2012; Caselli & Ceccarelli 2012; van Dishoeck et al. 2014; Matsumura et al. 2016; Sato et al. 2016). In the case of disks around solar-mass T Tauri stars, the H_2O snowline is calculated to exist at a few au from the central T Tauri star (e.g., Hayashi 1981). However, if we change the physical conditions such as the luminosity of the central star, the mass accretion rate, and the dust-grain size distribution in the disk, the location of the H_2O snowline will change (e.g., Du & Bergin 2014, Piso et al. 2015). Recent studies (Davis 2005; Garaud & Lin 2007; Min et al. 2011; Oka et al. 2011; Harsono et al. 2015; Mulders et al. 2015; Piso et al. 2015) calculate the evolution of the H_2O snowline in optically thick disks and show that it migrates as

---

the mass accretion rate in the disk decreases and as the dust grains grow in size. In some cases, the line may lie within the current location of Earth's orbit (1 au), meaning that the formation of water-devoid planetesimals in the terrestrial planet region becomes more difficult as the disk evolves. Sato et al. (2016) estimated the amount of icy pebbles accreted by terrestrial embryos after the H_2O snowline has migrated inwards to the distance of Earth's orbit (1 au). They argued that the fractional water content of the embryos is not kept below the current Earth's water content (0.023 wt%) unless the total disk size is relatively small (<100 au) and the disk has a stronger value of turbulence than that suggested by recent work, so that the pebble flow decays at early times. In contrast, other studies (Martin & Livio 2012, 2013) model the evolution of the H_2O snowline in a time-dependent disk with a dead zone and self-gravitational heating, and suggest that there is sufficient time and mass in the disk for the Earth to form from water-devoid planetesimals at the current location of Earth's orbit (1 au).

Ros & Johansen (2013) showed that around the H_2O snowline, dust-grain growth due to the condensation from millimeter to at least decimeter sized pebbles is possible on a timescale of only 1000 years. The resulting particles are large enough to be sensitive to concentration by streaming instabilities, pressure bumps, and vortices, which can cause further growth into planetesimals, even in young disks (<1 Myr, e.g., Zhang et al. 2015). Moreover, Banzatti et al. (2015) recently showed that the presence of the H_2O snowline leads to a sharp discontinuity in the radial profile of the dust emission spectral index, due to the replenishment of small grains through fragmentation because of the change in fragmentation velocities across the H_2O snowline. Furthermore, Okuzumi et al. (2016) argued that dust aggregates collisionally disrupt and pile up at the region slightly outside the snowlines due to the effects of sintering. These mechanisms of condensation (Ros & Johansen 2013; Zhang et al. 2015), fragmentation (Banzatti et al. 2015), and sintering (Okuzumi et al. 2016) of dust grains have been invoked to explain the multiple bright and dark ring patterns in the dust spectral index of the young disk HL Tau (ALMA Partnership et al. 2015).

Therefore, observationally measuring the location of the H_2O snowline is vital because it will provide information on the physical and chemical conditions of protoplanetary disks, such as the temperature and water vapor distribution in the disk midplane, and will give constraints on the current formation theories of planetesimals and planets. It will help clarify the origin of water on rocky planets including the Earth, since icy planetesimals, comets, and/or icy pebbles coming from outside the H_2O snowline may bring water to rocky planets including the Earth (e.g., Morbidelli et al. 2000, 2012; Caselli & Ceccarelli 2012; van Dishoeck et al. 2014; Matsumura et al. 2016; Sato et al. 2016).

Recent high spatial resolution direct imaging of protoplanetary disks at infrared wavelengths (e.g., Subaru/HiCIAO, VLT/SPHERE, Gemini South/GPI) and sub-millimeter wavelengths (e.g., the Atacama Large Millimeter/sub-millimeter Array [ALMA], the Sub-Millimeter Array) have revealed detailed structures in disks, such as the CO snowline (e.g., Mathews et al. 2013; Qi et al. 2013a, 2013b, 2015; Öberg et al. 2015), spiral structures (e.g., Muto et al. 2012; Benisty et al. 2015), strong azimuthal asymmetries in the dust continuum (e.g., Fukagawa et al. 2013; van der Marel et al. 2013, 2016),

gap structures (e.g., Walsh et al. 2014a; Akiyama et al. 2015; Rapson et al. 2015; Andrews et al. 2016; Nomura et al. 2016; Schwarz et al. 2016), and multiple axisymmetric bright and dark rings in the disk of HL Tau (ALMA Partnership et al. 2015). H_2O ice in disks has been detected by conducting low dispersion spectroscopic observations including the 3 μm H_2O ice absorption band (Pontoppidan et al. 2005; Terada et al. 2007), and crystalline and amorphous H_2O ice features at 63 μm (e.g., McClure et al. 2012, 2015). Multi-wavelength imaging including the 3 μm H_2O ice absorption band (Inoue et al. 2008) detected H_2O ice grains in the surface of the disk around the Herbig Ae/Be star, HD 142527 (Honda et al. 2009). More recently, Honda et al. (2016) reported the detection of H_2O ice in the HD 100546 disk, and postulated that photodesorption of water ice from dust grains in the disk surface can help explain the radial absorption strength at 3 μm. As we described previously, the H_2O snowline around a solar-mass T Tauri star is thought to exist at only a few au from the central star. Therefore, the required spatial resolution to directly locate the H_2O snowline is on the order of 10 mas (milliarcsecond) around nearby disks (∼100–200 pc), which remains challenging for current facilities.

In contrast, H_2O vapor has been detected through recent space spectroscopic observations of infrared rovibrational and pure rotational lines from protoplanetary disks around T Tauri stars and Herbig Ae stars using *Spitzer*/IRS (e.g., Carr & Najita 2008, 2011; Salyk et al. 2008, 2011; Pontoppidan et al. 2010a; Najita et al. 2013), *Herschel*/PACS (e.g., Fedele et al. 2012, 2013; Meeus et al. 2012; Riviere-Marichalar et al. 2012; Dent et al. 2013; Kamp et al. 2013; Blevins et al. 2016), and *Herschel*/HIFI (Hogerheijde et al. 2011; van Dishoeck et al. 2014, p. 835). van Dishoeck et al. (2013, 2014) reviewed the results of these recent space spectroscopic observations. The observations using *Spitzer*/IRS and *Herschel*/PACS are spatially unresolved; hence, large uncertainties remain on the spatial distribution of H_2O gas in the protoplanetary disk. Although the observations using *Herschel*/HIFI (Hogerheijde et al. 2011; van Dishoeck et al. 2014) have high spectral resolution (allowing some constraints on the radial location), they mainly probe the cold water vapor in the outer disk (beyond 100 au). The lines they detected correspond to the ground state rotational transitions, which have low upper state energies (see Section 3.2.3). Zhang et al. (2013) estimated the position of the H_2O snowline in the transitional disk around TW Hya by using the intensity ratio of H_2O lines with various wavelengths and upper state energies. They used archival spectra obtained by *Spitzer*/IRS, *Herschel*/PACS, and *Herschel*/HIFI. Blevins et al. (2016) investigated the surface water vapor distribution in four disks using data obtained by *Spitzer*/IRS and *Herschel*/PACS, and found that they have critical radii of 3–11 au, beyond which the surface gas-phase water abundance decreases by at least five orders of magnitude. The measured values for the critical radius are consistently smaller than the location of the surface H_2O snowline, as predicted by temperature profiles derived from the observed spectral energy distribution.

Studies investigating the structure of the inner disk from the analyses of velocity profiles of emission lines have been conducted using lines, such as the 4.7 μm rovibrational lines of CO gas (e.g., Goto et al. 2006; Pontoppidan et al. 2008, 2011). Profiles of emission lines from protoplanetary disks are usually affected by Doppler shift due to Keplerian rotation and thermal

broadening. Therefore, the velocity profiles of lines are sensitive to the radial distributions of molecular tracers in disks. Follow-up ground-based near- and mid-infrared (L, N band) spectroscopic observations of H_2O emission lines for some of the known brightest targets have been conducted using VLT/VISIR, VLT/CRIRES, Keck/NIRSPEC, and TEXES (a visitor instrument on Gemini North), and the velocity profiles of the lines have been obtained (e.g., Salyk et al. 2008, 2015; Pontoppidan et al. 2010b; Fedele et al. 2011; Mandell et al. 2012). These observations suggested that the water vapor resides in the inner disk, but the spatial and spectroscopic resolution is not sufficient to investigate the detailed structure, such as the position of the H_2O snowline. In addition, the lines they observed are sensitive to the disk surface temperature and are potentially polluted by slow disk winds, and they do not probe the midplane where planet formation occurs (e.g., Salyk et al. 2008; Pontoppidan et al. 2010b; Mandell et al. 2012; van Dishoeck et al. 2014). This is because these lines have large Einstein A coefficients and very high upper state energies (>3000 K), and exist in the near- to mid-infrared wavelength region where dust emission becomes optically thick in the surface regions (see also Section 3.2).

In this work, we seek candidate H_2O lines for locating the H_2O snowline through future high-dispersion spectroscopic observations. The outline of the paper is as follows. First, we calculate the chemical composition of a protoplanetary disk using a self-consistently derived physical model of a T Tauri disk to investigate the abundance and distribution of H_2O gas and ice, as opposed to assuming the position of the H_2O snowline. Second, we use the model results to calculate the velocity profiles of H_2O emission lines ranging in wavelength from near-infrared to sub-millimeter, and investigate the properties of H_2O lines which trace the emission from the hot water vapor within the H_2O snowline and are promising for locating the H_2O snowline. These calculations are explained in Section 2. The results and discussion are described in Section 3 and conclusions are listed in Section 4.

2. METHODS

2.1. The Physical Model of the Protoplanetary Disk

The physical structure of a protoplanetary disk model is calculated using the methods outlined in Nomura & Millar (2005) including X-ray heating as described in Nomura et al. (2007). In this subsection, we provide a brief overview of the physical model we adopt. A more detailed description of the background theory and computation of this physical model is described in the original papers (Nomura & Millar 2005; Nomura et al. 2007). Walsh et al. (2010, 2012, 2014b, 2015), Heinzeller et al. (2011), and Furuya et al. (2013) used the same physical model to study various chemical and physical effects, and they explain the treatment of the physical structure in detail.

We adopt the physical model of a steady, axisymmetric Keplarian disk surrounding a T Tauri star with mass $M_* = 0.5\,M_\odot$, radius $R_* = 2.0\,R_\odot$, and effective temperature $T_* = 4000$ K (Kenyon & Hartmann 1995). The α-disk model (Shakura & Sunyaev 1973) is adopted to obtain the radial surface density, assuming a viscous parameter of $\alpha = 10^{-2}$ and an accretion rate of $\dot{M} = 10^{-8}\,M_\odot$ yr^{-1}. The steady gas temperature and density distributions of the disk are computed self-consistently by solving the equations of hydrostatic

equilibrium in the vertical direction and the local thermal balance between gas heating and cooling. The heating sources of the gas are grain photoelectric heating by UV photons and heating due to hydrogen ionization by X-rays. The cooling mechanisms are gas-grain collisions and line transitions (for details, see Nomura & Millar 2005 and Nomura et al. 2007). The dust temperature distribution is obtained by assuming radiative equilibrium between absorption and reemission of radiation by dust grains. The dust heating sources adopted are the radiative flux produced by viscous dissipation (α-disk model) at the midplane of the disk, and the irradiation from the central star. The radial range for which the calculations are conducted is $r \sim 0.04$–305 au.

The dust properties are important because they affect the physical and chemical structure of protoplanetary disks in several ways (for details, see, e.g., Nomura & Millar 2005). Since dust grains are the dominant opacity source, they determine the dust temperature profile and the UV radiation field throughout the disk. Photodesorption, photodissociation, and photoionization processes are affected by the UV radiation field. The dust properties affect the gas temperature distribution, because photoelectric heating by UV photons is the dominant source of gas heating at the disk surface. The total surface area of dust grains has an influence on the chemical abundances of molecules through determining the gas and ice balance. In Appendix A, we describe a brief overview of the X-ray and UV radiation fields and the dust-grain models we adopt.

In Figure 1, we display the gas number density in cm^{-3} (top left), the gas temperature in K (top right, T_g), the dust-grain temperature in K (bottom left, T_d), and the wavelength-integrated UV flux in erg cm^{-2} s^{-1} (bottom right), as a function of disk radius in au and height (scaled by the radius, z/r). The density decreases as a function of disk radius and disk height with the densest region of the disk found in the disk midplane close to the star ($\sim 10^{14}$ cm^{-3}) and the most diffuse, in the disk surface at large radii ($\sim 10^5$ cm^{-3}), so that the density range in our adopted disk model covers almost 10 orders of magnitude. The gas temperature increases as a function of disk height and decreases as a function of disk radius with the hottest region found in the disk surface ($>10^3$ K), and the coldest region found in the outer disk (~ 10 K). In addition, due to the influence of viscous heating at the disk midplane, the temperature increases within several au from the central T Tauri star. In the disk surface, the dust-grain temperature is more than 10 times lower than the gas temperature. At low densities, gas-grain collisions become ineffective so the gas cools via radiative line transitions. In contrast, the gas and dust-grain temperatures are similar in the midplane region with high densities. Moreover, the disk surface closest to the parent star is subjected to the largest flux of both UV and X-ray photons, although the disk midplane is effectively shielded from UV and X-ray photons over the radial extent of our disk model.

2.2. Chemical Structure of the Protoplanetary Disk

In order to investigate the chemical structure of the protoplanetary disk, we use a large chemical network, which includes gas-phase reactions and gas-grain interactions (free-zeout of gas molecules on dust grains, and thermal and non-thermal desorption from dust grains). The non-thermal desorption mechanisms we adopt include cosmic-ray-induced desorption, and photodesorption by UV photons. Walsh et al.
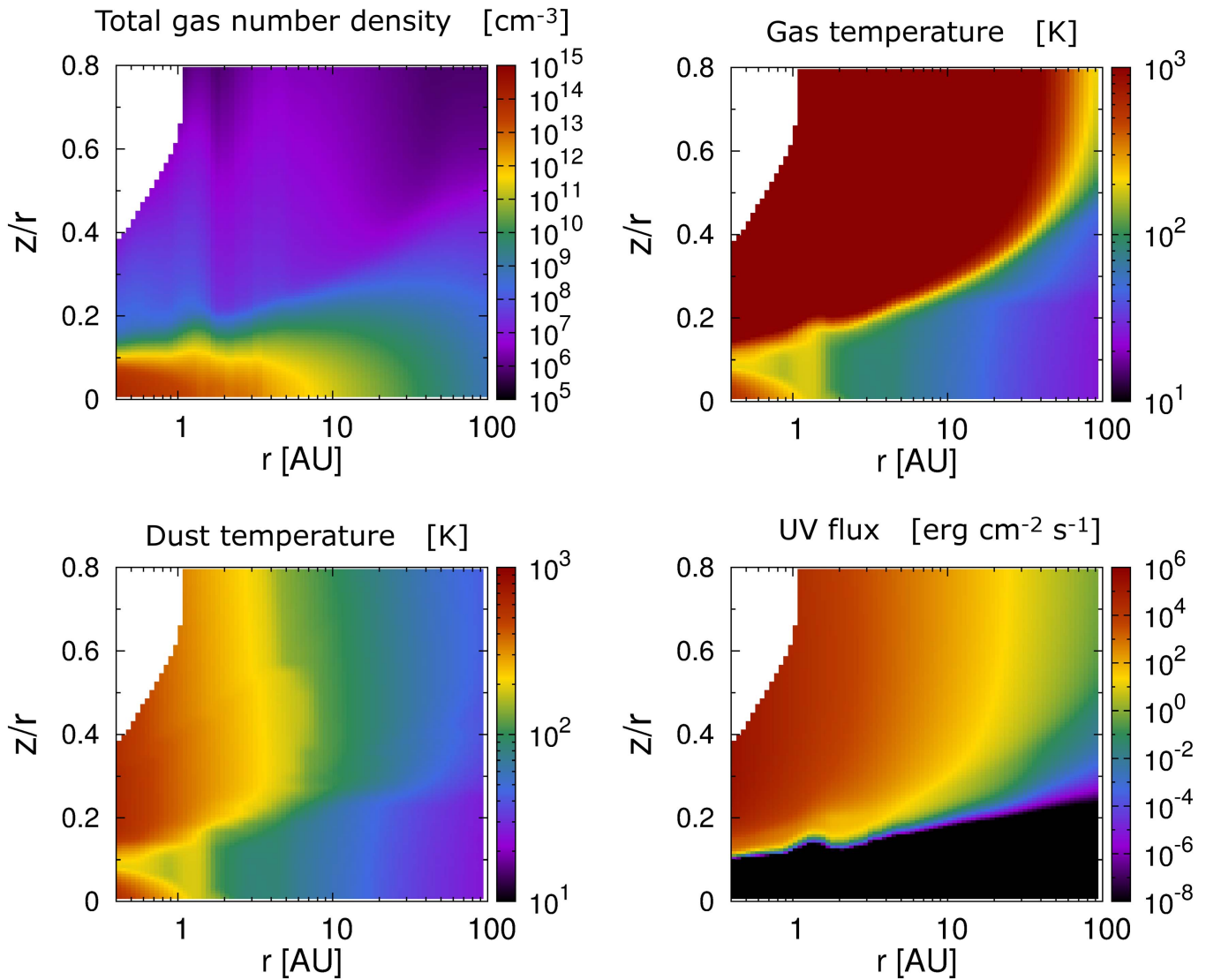
Figure 1. Total gas number density in cm^{-3} (top left), the gas temperature in K (top right), the dust temperature in K (bottom left), and the UV flux in erg cm^{-2} s^{-1} (bottom right) of a disk around a T Tauri star as a function of the disk radius in au and height (scaled by the radius, z/r) up to maximum radii of $r = 100$ au.

(2010, 2012, 2014b, 2015), Heinzeller et al. (2011), Furuya et al. (2013), Furuya & Aikawa (2014), Ishimoto et al. (2013), and Du & Bergin (2014) used similar chemical networks to calculate chemical structure of a protoplanetary disk, and they, and the reviews of Henning & Semenov (2013) and Dutrey et al. (2014), explain the background theories and procedures in detail. In this subsection, we outline the key points of the chemical network we use.

The addition of grain-surface chemistry (e.g., Hasegawa et al. 1992) is expected to aid the synthesis of complex organic molecules in the outer disk where significant freezeout has occurred. Some previous works on the chemical modeling of disks (e.g., Willacy 2007; Semenov & Wiebe 2011; Walsh et al. 2012, 2014b, 2015; Furuya et al. 2013; Drozdovskaya et al. 2014; Furuya & Aikawa 2014) have contained grain-surface reactions. However, the chemical network we adopt in this work does not contain such grain-surface reactions, and is equivalent to one of models in Walsh et al. (2010), which includes the same freezeout and desorption processes as those considered here. This is because we are primarily interested in the hot inner disk region where the molecular

line emission originates from the thermally desorbed gas reservoir.

2.2.1. Gas-phase Reactions

Our gas-phase chemistry is extracted from the UMIST Database for Astrochemistry (UDfA), henceforth referred to as "RATE06" (Woodall et al. 2007). Walsh et al. (2010, 2012) and Heinzeller et al. (2011) used RATE06 to calculate the chemical structure of a protoplanetary disk. We include almost the entire RATE06 gas-phase network, removing only those species (and thus reactions) that contain fluorine, F, and phosphorus, P, in order to reduce computation time. We have confirmed that the loss of F- and P-containing species has a minimal impact on the remaining chemistry (Walsh et al. 2010; Heinzeller et al. 2011). Our gas-phase network thus contains 375 atomic, molecular, and ionic species composed of the elements H, He, C, N, O, Na, Mg, Si, S, Cl, and Fe. Table 1 in the online material from Woodall et al. (2007) shows the list of these 375 species. The initial elemental fractional abundances (relative to total hydrogen nuclei density) we use are the set of oxygen-rich

<div align="center">

Table 1
Calculated Ortho-H_2O Line Parameters and Total Line Fluxes

</div>

$J_{K_a K_c}$	λ (μm)	Freq. (GHz)	A_{ul} (s^{-1})	E_{up} (K)	n_{cr} (cm^{-3})	Total Flux[a] (W m^{-2})
6_{43}–5_{50}	682.926	439.286	2.816×10^{-5}	1088.7	1.0×10^{6}	3.12×10^{-22}
8_{18}–7_{07}	63.371	4733.995	1.772	1070.6	1.5×10^{10}	5.66×10^{-18}
1_{10}–1_{01}	538.664	556.933	3.497×10^{-3}	61.0	2.9×10^{7}	1.13×10^{-20}

Note.

[a] In calculating total flux of these H_2O lines, we use a distance of $d = 140$ pc and the inclination angle of the disk is $i = 30°$.

low-metallicity abundances from Graedel et al. (1982), listed in Table 8 of Woodall et al. (2007). The chemical evolution is run for 10^6 years. By this time, the chemistry in the inner regions of the disk midplane inside the H_2O snowline is close to steady state, at which time the chemistry has forgotten its origins, justifying our use of initial elemental abundances, instead of ambient cloud abundances.

Our adopted reaction network consists of 4336 reactions including 3957 two-body reactions, 214 photoreactions, 154 X-ray/cosmic-ray-induced photoreactions, and 11 reactions of direct X-ray/cosmic-ray ionization. The adopted equations that give the reaction rates of two-body reactions, X-ray/cosmic-ray-induced photoreactions, and reactions of X-ray/cosmic-ray ionization are described in Section 2.1 of Woodall et al. (2007).

Here we mention that we use the previous version of the UDfA RATE06 (Woodall et al. 2007), instead of the latest version of UDfA, "RATE12" (McElroy et al. 2013). There are some updates in RATE12 such as reactions related to some complex molecules, and McElroy et al. (2013) described that the major difference between RATE12 and RATE06 is the inclusion of anion reactions. Although this has an influence on the abundances of carbon-chain molecules (Walsh et al. 2009; McElroy et al. 2013), it has little effect on the chemistry of main simple molecules, such as H_2O.

In our calculations of the chemistry, we have approximated our photoreaction rates at each point in the disk, $k^{ph}(r, z)$, by scaling the rates of RATE06, which assume the interstellar UV field, k_0, using the wavelength-integrated UV flux calculated at each point (see also Figure 1),

$$G_{FUV}(r, z) = \int_{912\,\text{Å}(13.6\,\text{eV})}^{2068\,\text{Å}(6\,\text{eV})} G_{FUV}(\lambda, r, z)d\lambda. \quad (1)$$

Using this value of $G_{FUV}(r, z)$, the rate for a particular photoreaction at each (r, z) is given by

$$k^{ph}(r, z) = \frac{G_{FUV}(r, z)}{G_0}k_0 \text{ s}^{-1}, \quad (2)$$

where G_0 is the interstellar UV flux (2.67×10^{-3} erg cm^{-2} s^{-1}, van Dishoeck et al. 2006).

2.2.2. Gas-grain Interactions

In our calculations, we consider the freezeout of gas-phase molecules on dust grains, and the thermal and non-thermal desorption of molecules from dust grains. For the thermal desorption of a molecule to occur, the dust-grain temperature must exceed the freezeout (sublimation) temperature of each molecule. Non-thermal desorption requires an input of energy from an external source and is thus independent of dust-grain temperature. The non-thermal desorption mechanisms we investigate are cosmic-ray-induced desorption (Leger et al. 1985; Hasegawa &

Herbst 1993) and photodesorption from UV photons (Westley et al. 1995; Willacy & Langer 2000; Öberg et al. 2007), as adopted in some previous studies (e.g., Walsh et al. 2010, 2012). In this subsection, we explain the mechanisms of freezeout and thermal desorption we use in detail. In Appendix B, we introduce the detailed mechanisms of non-thermal desporption we adopt (cosmic-ray-induced desorption and photodesorption from UV photons).

The freezeout (accretion) rate, k_i^a [s^{-1}], of species i onto the dust-grain surface is treated using the standard equation (e.g., Hasegawa et al. 1992; Woitke et al. 2009a; Walsh et al. 2010),

$$k_i^a = \alpha \sigma_d \langle v_i^{th} \rangle n_d \text{ s}^{-1}, \quad (3)$$

where α is the sticking coefficient, here assumed to be 0.4 for all species, which is in the range of high gas temperature cases ($T_g \sim 100$–200 K) reported in Veeraghattam et al. (2014). Previous theoretical and experimental studies suggested that the sticking coefficient tends to be lower as the gas and dust-grain temperature become higher (e.g., Masuda et al. 1998; Veeraghattam et al. 2014). $\sigma_d = \pi a^2$ is the geometrical cross section of a dust grain with radius, a, $\langle v_i^{th} \rangle$ is the thermal velocity of species i with mass m_i at gas temperature T_g, k_B is the Boltzmann's constant, and n_d is the number density of dust grains. We adopt the value of $\langle v_i^{th} \rangle = (k_B T_g/m_i)^{1/2}$ as Walsh et al. (2010) adopted. In this work, for our gas-grain interactions, we assume a constant grain radius of $a = 0.1$ μm and a fixed dust-grain fractional abundance ($x_d = n_d/n_H$)[8] of 2.2×10^{-12}, as previous studies adopted (e.g., Walsh et al. 2012). From the viewpoint of dust-grain surface area per unit volume, the adopted value of a constant grain radius a is consistent with the value from the dust-grain size distributions in the disk physical model adopted in this work (see also Appendix A). This adopted value of x_d is consistent with a gas-to-dust ratio of 100 by mass.

The thermal desorption rate, k_i^d [s^{-1}], of species i from the dust-grain surface is given by (e.g., Hasegawa et al. 1992; Woitke et al. 2009a; Walsh et al. 2010),

$$k_i^d = \nu_0(i)\exp\left(\frac{-E_d^K(i)}{T_d}\right) \text{s}^{-1}, \quad (4)$$

where $E_d^K(i)$ is the binding energy of species i to the dust-grain surface in units of K. The values of $E_d^K(i)$ for several important molecules are listed in Table 2. Most of these values are adopted in Walsh et al. (2010) or Walsh et al. (2012). T_d is the dust-grain temperature in units of K. The characteristic vibrational frequency of each adsorbed species i in its surface potential well, $\nu_0(i)$, is represented by a harmonic oscillator

---

[8] n_H is the total gas atomic hydrogen number density.

Table 2
Molecular Binding Energies

Species	Binding Energy $E_d^K(i)$ (K)	References
CO	855	1
CO_2	2990	2
H_2O	4820	3
CH_4	1080	4
N_2	790	1
NH_3	2790	5
HCN	4170	4
H_2CO	1760	6
C_2H_2	2400	4

References. (1) Öberg et al. (2005), (2) Edridge (2010), (3) Sandford & Allamandola (1993), (4) Yamamoto et al. (1983), (5) Brown & Bolina (2007), (6) Hasegawa & Herbst (1993).

relation (Hasegawa et al. 1992),

$$\nu_0(i) = \sqrt{\frac{2n_{\rm surf}E_d^{\rm erg}(i)}{\pi^2 m_i}} \ {\rm s}^{-1}, \qquad (5)$$

where, $E_d^{\rm erg}(i)$ is in units of erg here, m_i is the mass of each absorbed species i, and $n_{\rm surf} = 1.5 \times 10^{15}$ cm^{-2} is the surface density of absorption sites on each dust grain.

Considering these processes of freezeout, thermal desorption, cosmic-ray-induced desorption, and photodesorption, the total formation rate of ice species i is

$$\dot{n}_{i,\rm ice} = n_i k_i^a - n_{i,\rm ice}^{\rm desorb}(k_i^d + k_i^{\rm crd} + k_i^{\rm pd}). \qquad (6)$$

where $k_i^{\rm crd}$ is the cosmic-ray-induced thermal desorption rate for each species i, $k_i^{\rm pd}$ is the photodesorption rate for a specific species i, $n_{i,\rm ice}$ denotes the number density of ice species i, and $n_{i,\rm ice}^{\rm desorb}$ is the fraction of $n_{i,\rm ice}$ located in the uppermost active surface layers of the ice mantles. The value of $n_{i,\rm ice}^{\rm desorb}$ is given by (Aikawa et al. 1996; Woitke et al. 2009a)

$$n_{i,\rm ice}^{\rm desorb} = \begin{cases} n_{i,\rm ice} & (n_{\rm ice} < n_{\rm act}), \\ n_{\rm act}\dfrac{n_{i,\rm ice}}{n_{\rm ice}} & (n_{\rm ice} \geqslant n_{\rm act}), \end{cases} \qquad (7)$$

where $n_{\rm ice}$ is the total number density of all ice species, $n_{\rm act} = 4\pi a^2 n_d n_{\rm surf} N_{\rm Lay}$ is the number of active surface sites in the ice mantle per volume. $N_{\rm Lay}$ is the number of surface layers to be considered as "active," and we adopt the value from Aikawa et al. (1996), $N_{\rm Lay} = 2$.

2.3. Profiles of H_2O Emission Lines from Protoplanetary Disks

Using the H_2O gas abundance distribution obtained from our chemical calculations described in Section 2.2, we calculate the profiles of H_2O emission lines ranging from near-infrared to sub-millimeter wavelengths, and investigate which lines are the best candidates for probing emission from the inner thermally desorbed water reservoir, i.e., within the H_2O snowline. We also study how the line flux and profile shape depends upon the location of the H_2O snowline. In the following paragraphs, we outline the calculation methods used to determine the H_2O emission line profiles (based on Rybicki & Lightman 1986; Hogerheijde & van der Tak 2000, and Nomura & Millar 2005).

Here we define the transition frequency of each line as ν_{ul}, where the subscript ul means the transition from the upper level (u) to the lower level (l). The intensity of each line profile at the frequency ν, $I_{ul}(\nu)$, is obtained by solving the radiative transfer equation in the line-of-sight direction of the disk,

$$\frac{{\rm d}I_{ul}(\nu)}{{\rm d}s} = -\chi_{ul}(\nu)(I_{ul}(\nu) - S_{ul}(\nu)). \qquad (8)$$

The source function, $S_{ul}(\nu)$, and the total extinction coefficient, $\chi_{ul}(\nu)$, are given by

$$S_{ul}(\nu) = \frac{1}{\chi_{ul}(\nu)} n_u A_{ul} \Phi_{ul}(\nu) \frac{h\nu_{ul}}{4\pi}, \qquad (9)$$

and

$$\chi_{ul}(\nu) = \rho_d \kappa_{ul} + (n_l B_{lu} - n_u B_{ul})\Phi_{ul}(\nu)\frac{h\nu_{ul}}{4\pi}, \qquad (10)$$

where the symbols A_{ul} and B_{ul} are the Einstein A and B coefficients for the transition $u \to l$, the symbol B_{lu} is the Einstein B coefficient for the transition $l \to u$, h is the Planck constant, and n_u and n_l are the number densities of the upper and lower levels, respectively. The energy difference between the levels u and l corresponds to $h\nu_{ul}$. ρ_d is the mass density of dust grains, which we calculate from the values of the total gas mass density ρ_g and the gas-to-dust mass ratio ($\rho_g/\rho_d = 100$). κ_{ul} is dust absorption coefficient at the frequency ν_{ul} as described in Section 2.1.

The symbol $\Phi_{ul}(\nu)$ is the line profile function at the frequency ν, and we consider the Doppler shift due to Keplerian rotation and thermal broadening, in calculating the emission line profiles. This function is given by

$$\Phi_{ul}(\nu) = \frac{1}{\Delta\nu_D\sqrt{\pi}}\exp\left[-\frac{(\nu + \nu_K - \nu_{ul})^2}{\Delta\nu_D^2}\right], \qquad (11)$$

where $\Delta\nu_D = (\nu_{ul}/c)(\sqrt{2kT_g/m})$ is the Doppler width, c is the speed of light, T_g is the gas temperature, k is the Boltzmann constant, m is the mass of a water molecule, and ν_K is the Doppler shift due to the projected Keplerian velocity for the line-of-sight direction and is given by,

$$\nu_K = \frac{\nu_{ul}}{c}\sqrt{\frac{GM_*}{r}}\sin\phi\sin i, \qquad (12)$$

where G is the gravitational constant, M_* is the mass of central star, r is the distance from the central star, ϕ is the azimuthal angle between the semimajor axis and the line that links the point in the disk along the line of sight and the center of the disk.

The observable profiles of flux density are obtained by integrating Equation (8) in the line-of-sight direction and summing up the integrals in the plane of the projected disk, (x, y), as

$$F_{ul}(\nu) = \frac{1}{4\pi d^2}\int d\Omega \int\int dx dy \int_{-s_\infty}^{s_\infty} j_{ul}(s, x, y, \nu)ds, \qquad (13)$$

where d is the distance of the observed disk from the Earth. $j_{ul}(s, x, y, \nu)$ is the emissivity at (s, x, y) and the frequency ν considering the effect of absorption in the upper disk layer and

it is given by the following equation,

$$j_{ul}(s, x, y, \nu) = n_u(s, x, y) A_{ul} \frac{h\nu_{ul}}{4\pi} \Phi_{ul}(s, x, y, \nu)$$
$$\times \exp(-\tau_{ul}(s, x, y, \nu)), \qquad (14)$$

and $\tau_{ul}(s, x, y, \nu)$ is the optical depth from s to the disk surface s_∞ at the frequency ν given by,

$$\tau_{ul}(s, x, y, \nu) = \int_s^{s_\infty} \chi_{ul}(s', x, y, \nu) ds'. \qquad (15)$$

Hence, the observable total flux of the lines, F_{ul}, are given by the following equation,

$$F_{ul} = \int F_{ul}(\nu) d\nu \qquad (16)$$

Here, we use a distance of $d = 140$ pc for calculating the line profiles since this is the distance to the Taurus molecular cloud, one of the nearest star formation regions with observable protoplanetary disks.

The code for ray tracing, which we have built for calculating emission line profiles from the protoplanetary disk, is a modification of the original 1D code called RATRAN[9] (Hogerheijde & van der Tak 2000). We adopt the data for the ortho- and para-H_2O energy levels from Tennyson et al. (2001), the radiative rates (Einstein A coefficients A_{ul}) from the BT2 water line list (Barber et al. 2006), and the collisional rates, $\langle \sigma v \rangle$, for the excitation of H_2O by H_2 and by electrons from Faure & Josselin (2008). We use the collisional rates to determine the critical densities of transitions of interest. These data are part of the Leiden Atomic and Molecular Database called LAMDA[10] (Schöier et al. 2005). The level populations of the water molecule (n_u and n_l) are calculated under the assumption of local thermal equilibrium (LTE). In Section 3.2.5, we discuss the validity of the assumption of LTE in our work. We do not include dust-grain emission nor emission from disk winds and jet components in calculating the emission line profiles. However, we do include the effects of the absorption of line emission by dust grains (as described above).

The nuclear spins of the two hydrogen atoms in each water molecule can be either parallel or anti-parallel, and this results in a grouping of the H_2O energy levels into ortho ($K_a + K_c =$ odd) and para ($K_a + K_c =$ even) ladders. The ortho to para ratio (OPR) of water in the gas gives information on the conditions, formation, and thermal history of water in specific regions, such as comets and protoplanetary disks (e.g., Mumma & Charnley 2011; van Dishoeck et al. 2013, 2014). An alternative way to describe the OPR is through the "spin temperature," defined as the temperature that characterizes the observed OPR if it is in thermal equilibrium. The OPR becomes zero in the limit of low temperature and three in the limit of high temperature ($\gtrsim 60$ K). The original definition of OPR of water vapor in thermal equilibrium is described in Mumma et al. (1987). In this paper, we set the OPR = 3 throughout the disk to calculate values of n_u and n_l from the H_2O gas abundance distribution. The lines we calculate in order to locate the position of the H_2O snowline mainly trace the hot water vapor for which the temperature is higher than the water sublimation temperature ($\sim$150–160 K). The disk
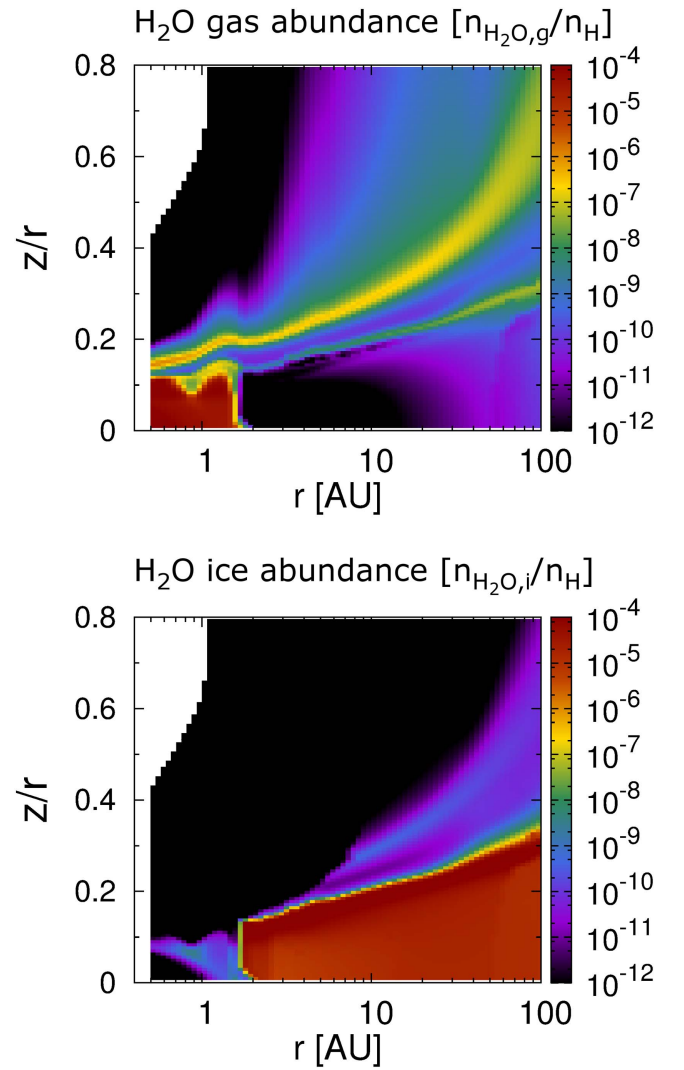
Figure 2. Fractional abundance (relative to total hydrogen nuclei density) distributions of H_2O gas (top) and H_2O ice (bottom) of a disk around a T Tauri star as a function of disk radius and height (scaled by the radius, z/r) up to maximum radii of $r = 100$ au.

physical structure of our adopted model is steady, and thermal and chemical equilibrium is mostly achieved throughout the disk. In addition, previous observational data on warm water detected at mid-infrared wavelengths in the inner regions of protoplanetary disks are consistent with OPR = 3 (e.g., Pontoppidan et al. 2010a).

Here we also mention that Hama et al. (2016) reported from their experiments that water desorbed from the icy dust-grain surface at 10 K shows the OPR = 3, which invalidates the assumed relation between OPR and the formation temperature of water. They argue that the role of gas-phase processes that convert the OPR to a lower value in low temperature regions is important, though the detailed mechanism is not yet understood.

3. RESULTS AND DISCUSSION

3.1. The Distributions H_2O Gas and Ice

Figure 2 shows the fractional abundances (relative to total gas hydrogen nuclei density, n_H) of H_2O gas and H_2O ice in a disk around a T Tauri star as a function of disk radius r and height scaled by the radius (z/r). The radial range over which

the chemistry is computed is $r \sim 0.5$ and 100 au in order to reduce computation time. Here we mention that at small radii, due to the high densities found in the midplane, there is a significant column density of material shielding this region from the intense UV and X-ray fields of the star. Therefore, molecules are expected to survive in the midplane at radii within ~ 0.1 au, unless there are cavities in the dust and gas. Thus the actual total amount of molecular gas in the inner disk may be larger than that of our chemical calculation results.

According to this figure, the fractional abundance with respect to H_2 of H_2O gas is high ($\sim 10^{-4}$) in the midplane region inside the H_2O snowline, and, in contrast, it is low ($\lesssim 10^{-12}$) in the midplane outside the H_2O snowline. The fractional abundance of H_2O ice has the opposite distribution. It is low ($\lesssim 10^{-9}$) in the midplane region inside the H_2O snowline, and, in contrast, it is high ($\sim 10^{-5}$) in the midplane outside the H_2O snowline. The H_2O snowline in the T Tauri disk that we adopt in this work exists at a radius of ~ 1.6 au in the midplane ($T_g \sim 150$–160 K), consistent with the binding energy we adopt.

Inside the H_2O snowline, the temperature exceeds the sublimation temperature under the pressure conditions of the midplane ($T_g \sim 150$–160 K) and most of the H_2O is released into the gas-phase through thermal desorption. In addition, this region is almost completely shielded from intense UV and X-ray fields of the star and interstellar medium (Nomura & Millar 2005; Nomura et al. 2007, see also Figure 2 of Walsh et al. 2012), has a high temperature (>150 K) and large total gas particle number density ($>10^{11}$ cm^{-3}), and thermal equilibrium between the gas and dust is achieved ($T_g \sim T_d$). Under these conditions, the gas-phase chemistry is close to thermochemical equilibrium and most of the oxygen atoms will be locked up into H_2O (and CO) molecules (e.g., Glassgold et al. 2009; Woitke et al. 2009a, 2009b; Walsh et al. 2010, 2012, 2015; van Dishoeck et al. 2013, 2014; Du & Bergin 2014; Antonellini et al. 2015). Therefore, the H_2O gas abundance of this region is approximately given by the elemental abundance of oxygen (1.76×10^{-4}, Woodall et al. 2007) minus the fraction bound in CO.

In addition, the fractional abundance of H_2O gas is relatively high in the hot surface layer of the outer disk. First, at z/r of 0.1–0.3 between $r \sim 0.5$ and 100 au, the fractional abundance of H_2O gas is $\sim 10^{-8}$–10^{-7}. This region can be considered as the sublimation (photodesorption) front of H_2O molecules, driven by the relatively strong stellar UV radiation. This so-called photodesorbed layer (Dominik et al. 2005) allows H_2O to survive in the gas phase where it would otherwise be frozen out on the dust-grain surfaces. The abundance and extent of gas-phase H_2O in this layer is mediated by absorption back onto the dust grain, destruction by the stellar UV photons and by chemical reactions with other species.

Second, at z/r of 0.15–0.7 between $r \sim 0.5$ and 100 au, the H_2O abundance is relatively high ($\sim 10^{-7}$) compared with the cold midplane region of the outer disk ($\lesssim 10^{-12}$–10^{-10}). Since the gas temperature is significantly higher than the dust temperature (typically $T_g \sim 200$–2000 K) and the gas density is low compared to the disk midplane, the water chemistry is controlled by chemical kinetics as opposed to thermodynamic (or chemical) equilibrium. Due to the very high gas temperature (>200 K), the energy barriers for the dominant neutral-neutral reactions of $O + H_2 \rightarrow OH + H$ and $OH + H_2 \rightarrow H_2O + H$ are readily surpassed and gaseous H_2O is produced rapidly.
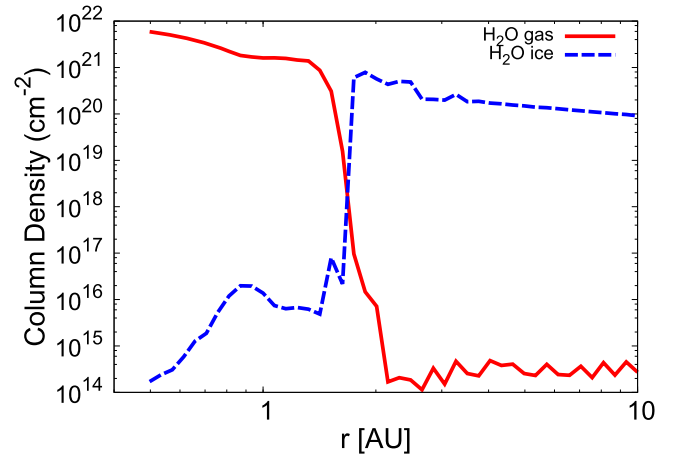
Figure 3. Radial profile of the vertically integrated column density cm^{-2} of H_2O gas (red solid line) and ice (blue dashed line).

This route will drive all the available gas-phase oxygen into H_2O, unless strong UV or a high atomic hydrogen abundance is able to convert some water back to OH and O (e.g., Glassgold et al. 2009; Woitke et al. 2009b; Meijerink et al. 2012; van Dishoeck et al. 2013, 2014; Walsh et al. 2015). In the uppermost surface layers, H_2O is even more rapidly destroyed by photodissociation and reactions with atomic hydrogen than it is produced, so there is little water at the very top of the disk. The OH gas abundance in our calculations and others (e.g., Walsh et al. 2012) is high in this hot surface region. It is consistent with the above discussions that neutral-neutral reactions including OH and H_2O are dominant and strong UV or a high atomic hydrogen abundance converts some water back to OH and O (Walsh et al. 2012, 2015).

Figure 3 shows the radial column density profile of H_2O gas (red solid line) and ice (blue dashed line). The column density of H_2O gas and ice in the disk midplane flips across the H_2O snowline (~ 1.6 au). The column density of H_2O gas is high ($\sim 10^{21}$ cm^{-2}) inside the H_2O snowline, and, in contrast, is low outside the H_2O snowline ($\sim 10^{14}$–10^{15} cm^{-2}). The column density profile of H_2O ice is roughly opposite. The column density of H_2O ice in the outer disk is $\sim 10^{20}$–10^{21} cm^{-2}. Previous chemical modeling calculations (e.g., Walsh et al. 2012, 2015; Du & Bergin 2014) gave a column density of H_2O gas inside the H_2O snowline of around 10^{21}–10^{22} cm^{-2}. This value is slightly higher than in our calculations, possibly due to the inclusion of grain-surface reactions. However, since gas-phase H_2O in the disk midplane is likely obscured by dust grains at near- to mid-infrared wavelengths (Walsh et al. 2015), the "visible" H_2O gas column density at these wavelength is much smaller than the actual amount. For example, in Walsh et al. (2015), the visible value is on the order of a few times 10^{19} cm^{-2} within the H_2O snowline. Previous infrared low dispersion spectroscopic observations using *Spitzer*/IRS for classical T Tauri stars derive the H_2O gas column densities ranging from 4×10^{17} to 7.9×10^{20} cm^{-2} (Carr & Najita 2011; Salyk et al. 2011). Despite the model T Tauri disk being a generic model that is not representative of any particular source, there is significant overlap between the calculated "visible" column densities and these observed values, though it should be acknowledged that there is a three orders-of-magnitude spread in the observed values.

Previous analytical models and numerical simulations derived the position of the H_2O snowline of an optically thick disk for given parameters, such as mass (M_*) and temperature (T_*) of the central star, a viscous parameter α, an accretion rate $\dot{M}$, a gas-to-dust mass ratio g/d, and the average dust-grain size a and opacity (e.g., Davis 2005; Garaud & Lin 2007; Min et al. 2011; Oka et al. 2011; Du & Bergin 2014; Harsono et al. 2015; Mulders et al. 2015; Piso et al. 2015), and suggested that the position of the H_2O snowline changes as these parameters change. In the case of T Tauri disks with $M_* \sim 0.5$–$1\,M_\odot$, $\dot{M} \sim 10^{-8}\,M_\odot\ \mathrm{yr}^{-1}$, and $a \sim 0.1\,\mu$m, the position of the H_2O snowline is ~ 1.5–2 au. In our calculations, we use similar parameters for M_*, $\dot{M}$, and a, and the H_2O snowline appears at a radius of around 1.6 au in the midplane ($T_g \sim 150$–160 K), which is in the range of previous works.

Heinzeller et al. (2011) investigated the effects of physical mass transport phenomena in the radial direction by viscous accretion and in the vertical direction by diffusive turbulent mixing and disk winds. They showed that the gas-phase H_2O abundance is enhanced in the warm surface layer due to the effects of vertical mixing. In contrast, they mentioned that the gas-phase H_2O abundance in the midplane inside the H_2O snowline is not affected by the accretion flow, since chemical reactions are considered to be fast enough in this region to compensate for the effects of the accretion flow.

3.2. H_2O Emission Lines from Protoplanetary Disks

We perform ray-tracing calculations and investigate the profiles of H_2O emission lines for a protoplanetary disk in Keplerian rotation, using the methods described in Section 2.3 and the next paragraph. We include rovibrational and pure rotational ortho- and para- H_2O lines at near-, mid-, and far-infrared and sub-millimeter wavelengths, and find that H_2O lines, which have small Einstein A coefficients ($A_{ul} \sim 10^{-3}$–10^{-6} s^{-1}) and relatively high upper energy levels ($E_{up} \sim 1000$ K), are most promising for tracing emission from the innermost hot water reservoir within the H_2O snowline.

Here we describe how we find 50 candidate lines, which are selected from the LAMDA database of H_2O transition lines. First of all, we proceeded by selecting about 20 H_2O lines from the LAMDA database, which have various wavelengths (from near-infrared to sub-millimeter), Einstein A coefficients ($A_{ul} \sim 10^{-1}$–10^{-7} s^{-1}), and upper state energies ($E_{up} < 3000$ K). In making this initial selection, we ignored lines with very small Einstein A coefficients and very high upper state energies, since the emission fluxes of these lines are likely too weak to detect. When we calculated the profiles of these lines, we noticed that H_2O lines with small Einstein A coefficients ($A_{ul} \sim 10^{-3}$–10^{-6} s^{-1}) and relatively large upper state energies ($E_{up} \sim 700$–2100 K) are the best candidates to trace emission from the hot water reservoir within the H_2O snowline. The number of these candidate lines is 10 lines within the originally selected 20 lines. Then we searched all other ortho-H_2O transition lines that satisfy these conditions and found an additional 40 ortho-H_2O candidate water lines.

In the remaining subsections, we describe the detailed properties of three characteristic pure rotational ortho-H_2O lines ($\lambda = 682.93$, 63.37, $538.66\,\mu$m). These three lines have different values of A_{ul} and E_{up}. We find that the H_2O 682.93 μm line, which falls in ALMA band 8 (see Section 3.2.6), is a candidate for tracing emission from the innermost hot water reservoir within the H_2O snowline. The 63.37 and 538.66 μm lines are examples of lines that are less suited to trace emission from water vapor within the H_2O snowline. We consider these two particular lines to test the validity of our model calculations, since the fluxes of these two lines from protoplanetary disks are observed with *Herschel* (see Sections 3.2.2, 3.2.3). The list of suitable lines from mid-infrared (Q band) to sub-millimeter, and their properties, especially the variation in line fluxes with wavelength, are described in detail in our companion paper (Paper II, S. Notsu et al. 2016, in preparation).

3.2.1. The Case of a Suitable H_2O Emission Line to Trace Emission from the Hot Water Reservoir within the H_2O Snowline

The top panels in Figure 4 show the emission profiles of three pure rotational ortho-H_2O lines at $\lambda = 682.93\,\mu$m ($J_{K_a K_c} = 6_{43}$–5_{50}, top left), $63.37\,\mu$m ($J_{K_a K_c} = 8_{18}$–7_{07}, top middle), and $538.66\,\mu$m ($J_{K_a K_c} = 1_{10}$–1_{01}, top right), which have various Einstein A coefficients (A_{ul}) and upper state energies (E_{up}). The detailed parameters, such as transitions ($J_{K_a K_c}$), wavelength, frequency, A_{ul}, E_{up}, critical density n_{cr}, and total line fluxes of these three H_2O lines are listed in Table 1. In calculating these profiles, we assume that the distance d to the object is 140 pc (approximately the distance of Taurus molecular cloud), and the inclination angle i of the disk is 30°. The total fluxes of these three lines ($\lambda = 682.93$, 63.37, $538.66\,\mu$m) are 3.12×10^{-22}, 5.66×10^{-18}, 1.13×10^{-20} W m^{-2}, respectively. The bottom panels in Figure 4 show the velocity profiles of the H_2O 63.37 μm line (bottom left) and the 538.66 μm line (bottom right), which enlarge the inner components.

Since the H_2O lines at $\lambda = 682.93$ and $63.37\,\mu$m have large upper state energies ($E_{up} = 1088.7$ and 1070.6 K), these lines trace the hot water vapor ($T_g \gtrsim$ a few hundred K). On the basis of the results of our chemical calculations, the abundance of H_2O gas is high in the optically thick hot inner region within the H_2O snowline near the equatorial plane ($T_g > 150$ K) and in the hot optically thin surface layer of the outer disk.

In the top left panel of Figure 4, we show the H_2O line emission at 682.93 μm. The contribution from the optically thin surface layer of the outer disk (black dashed line, 2–30 au, "out" component) is very small compared with that from the optically thick region near the midplane of the inner disk (red solid line, 0–2 au, "in" component). This is because this H_2O 682.93 μm line has a small A_{ul} (=2.816×10^{-5} s^{-1}). On the basis of Equations (13)–(16) in Section 2.3, the observable flux density is calculated by summing up the emissivity at each point ($j_{ul}(s, x, y, \nu)$) in the line-of-sight direction. In the optically thin ($\tau_{ul} \ll 1$) region (e.g., the disk surface layer), the flux density is roughly characterized by integrating the values of $n_u(s, x, y)A_{ul}$ at each point. On the other hand, in the optically thick ($\tau_{ul} \gtrsim 1$) region (e.g., the disk midplane of the inner disk), the flux density is independent of $n_u(s, x, y)$ and A_{ul} at each point, and it becomes similar to the value of the Planck function at T_g around the region of $\tau_{ul} \sim 1$. Therefore, the emission profile of the H_2O 682.93 μm line, which has a small A_{ul} and a relatively high E_{up}, mainly traces the hot H_2O gas inside the H_2O snowline and shows the characteristic double-peaked profile due to Keplerian rotation. In this profile, the position of the two peaks and the rapid drop in flux density between the peaks give information on the distribution of hot H_2O gas within the H_2O snowline. This profile potentially contains information that can be used to determine the H_2O snowline position. The spread in the wings of the emission profile (high velocity regions) represents the inner edge of the H_2O gas distribution in the disk. This is because emission from
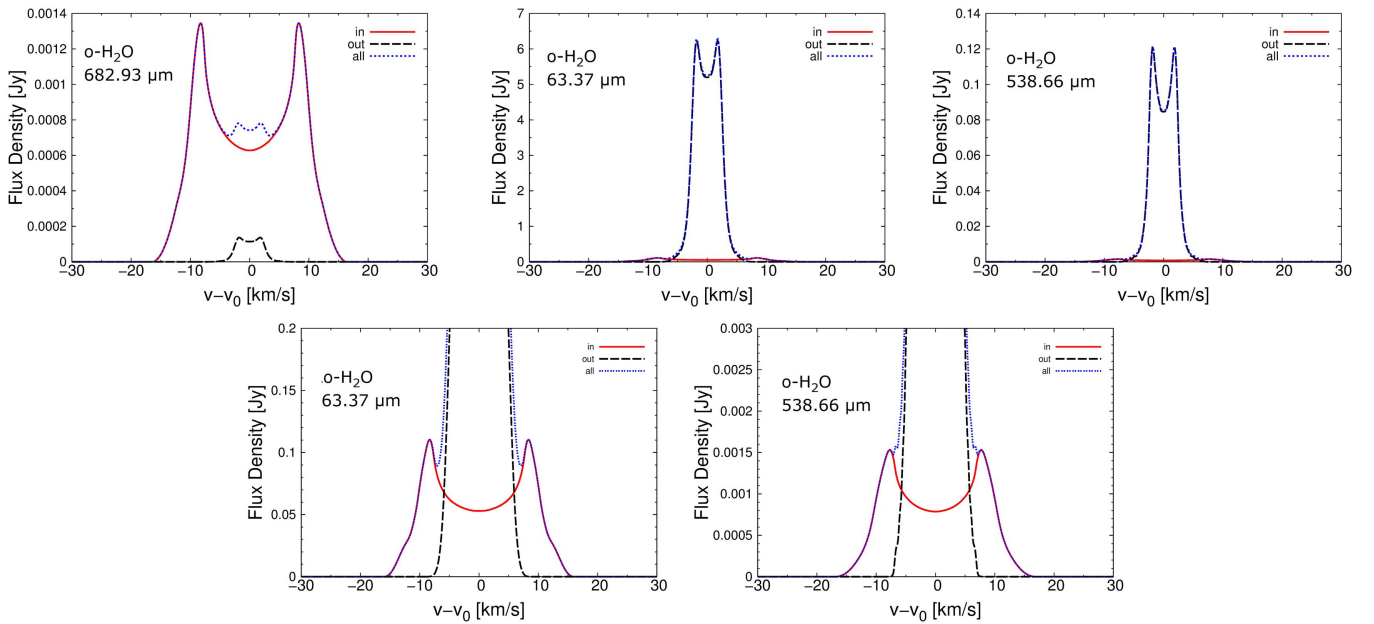
Figure 4. Top: velocity profiles of three characteristic pure rotational ortho-H_2O lines at $\lambda = 682.93\ \mu m$ ($J_{K_aK_c} = 6_{43}-5_{50}$, top left), 63.37 μm ($J_{K_aK_c} = 8_{18}-7_{07}$, top middle), and 538.66 μm ($J_{K_aK_c} = 1_{10}-1_{01}$, top right), which have various Einstein A coefficients A_{ul} and upper state energies E_{up}. Bottom: velocity profiles of the ortho-H_2O 63.37 μm line (bottom left) and 538.66 μm line (bottom right), which enlarge the inner components. *Red solid lines* are the emission line profiles from inside 2 au (~inside the H_2O snowline), *black dashed lines* are those from 2 au to 30 au (approximately outside the H_2O snowline), and *blue dotted lines* are those from the total area inside 30 au. In calculating these profiles, we assume that the distance to the object d is 140 pc (approximately the distance of the Taurus molecular cloud), and the inclination angle of the disk i is 30°.

each radial region in the disk is Doppler-shifted due to the Keplerian rotation. Because the area near the outer emitting region is larger than that of the inner region ($\propto r^2$), the contribution to the emission from the region near the outer edge is larger if the emissivity at each radial point is similar.

Figure 5 shows the line-of-sight emissivity distributions of these three pure rotational ortho-H_2O lines. Figure 6 shows the total optical depth (gas emission and dust) distributions for the same transitions. We assume that the inclination angle, i, of the disk is 0° in making these figures, and thus the line-of-sight direction is from $z = +\infty$ to $-\infty$ at each disk radius. According to the top panels of Figures 5 and 6, the values of the emissivity at $r < 1.6$ au (the position of the H_2O snowline) and $z/r \sim 0.1$ are higher than that of the other regions, including the optically thin hot surface layer of the outer disk and the photodesorbed layer. Although we cannot detect the emission from $z \sim 0$ because of the high optical depth of the inner disk midplane due to the absorption by dust grains and excited H_2O molecules, we can get information about the distribution of hot H_2O gas within the H_2O snowline. This is because the H_2O gas fractional abundance is close to constant within $r < 1.6$ au (the position of the H_2O snowline) and $z/r \sim 0$–0.1 (see also Section 3.1 and Figure 2).

3.2.2. The Case of a H2O Emission Line That Traces the Hot Surface Layer

In the top middle panel of Figure 4, where we show the line profile for the H_2O 63.37 μm line, the contribution from the optically thin surface layer of the outer disk (black dashed line, 2–30 au, "out" component) is large compared with that of the optically thick region near the midplane of the inner disk (red solid line, 0–2 au, "in" component), and the shape of the line profile is a much narrower double-peaked profile. This is because this H_2O 63.37 μm line has a large A_{ul} (=1.772 s^{-1}),

though E_{up} (=1070.6 K) is similar to that of the H_2O 682.93 μm line (=1088.7 K), and thus the flux density from the hot surface layer of the outer disk becomes strong. Here we note that since the peak velocities of the "in" and "out" components are different, water lines with large A_{ul} at infrared wavelengths, such as the H_2O 63.37 μm line, can in principal trace the hot H_2O gas within the H_2O snowline. However, there is no current or future instrument with enough sensitivity and spectral resolution to distinguish the peaks of the "in" component from the "out" component in these lines. For example, SPICA/SAFARI is a future instrument with far-infrared spectrograph, but its spectral resolution is low ($R \sim 3000$) and is not enough to distinguish the peaks of these line profiles. The difference in the peak flux density is very large ($\gtrsim$ several tens) and the wings of both components are blended (see also the bottom left panel of Figure 4).

According to the middle panels of Figures 5 and 6, the values of the emissivity at each (r, z) point in the optically thin hot surface layer of the outer disk and the photodesorbed layer are as strong as that of the optically thick region inside the H_2O snowline. For similar reasons as the case for the 682.93 μm line, emission from the outer part of the emitting region in the disk dominates. In addition, the outer disk midplane opacity of this line is larger than that of the H_2O 682.93 μm line, because the dust opacity becomes large at shorter wavelengths (e.g., Nomura & Millar 2005).

We mention that previous space far-infrared low dispersion spectroscopic observations with *Herschel*/PACS ($R \sim 1500$) detected this line from some T Tauri disks and Herbig Ae disks (e.g., Fedele et al. 2012, 2013; Meeus et al. 2012; Riviere-Marichalar et al. 2012; Dent et al. 2013). Although the profiles of these lines are unresolved, comparison with models indicates that the emitting regions of these observations are thought to originate in the hot surface layer (e.g., Fedele et al. 2012;
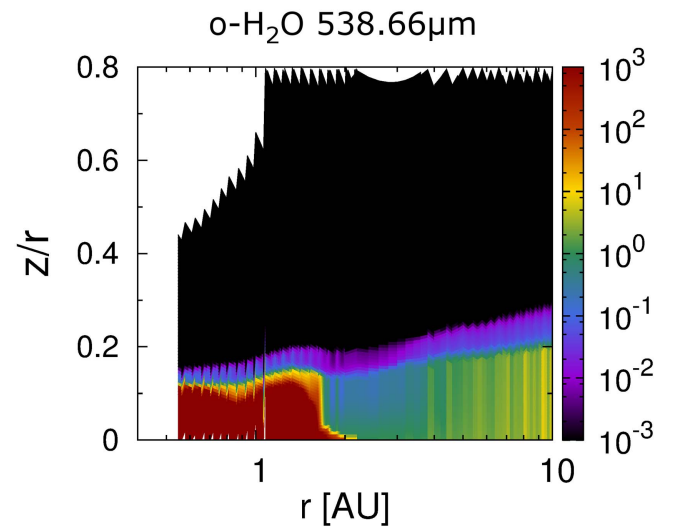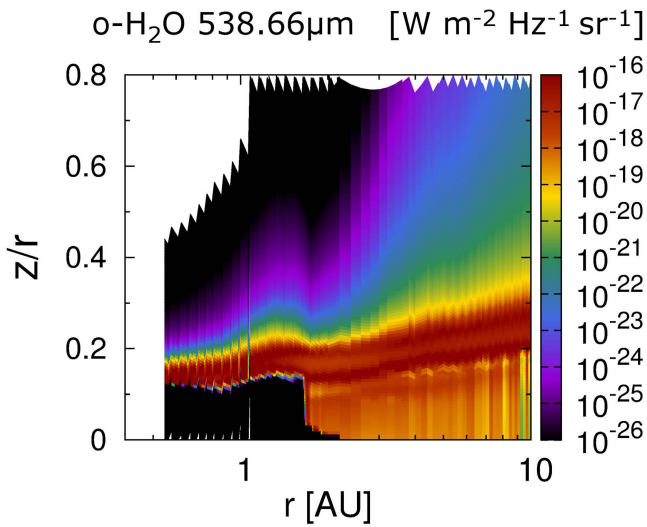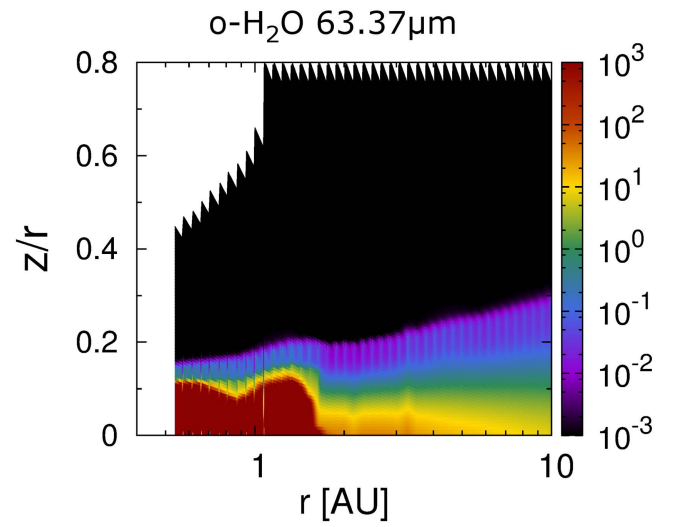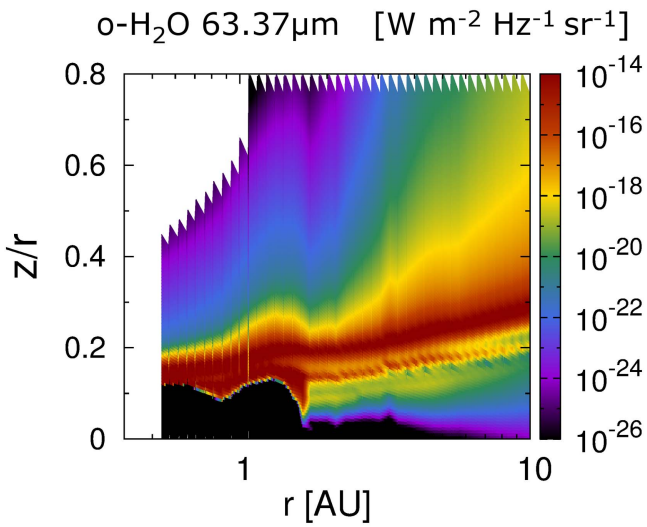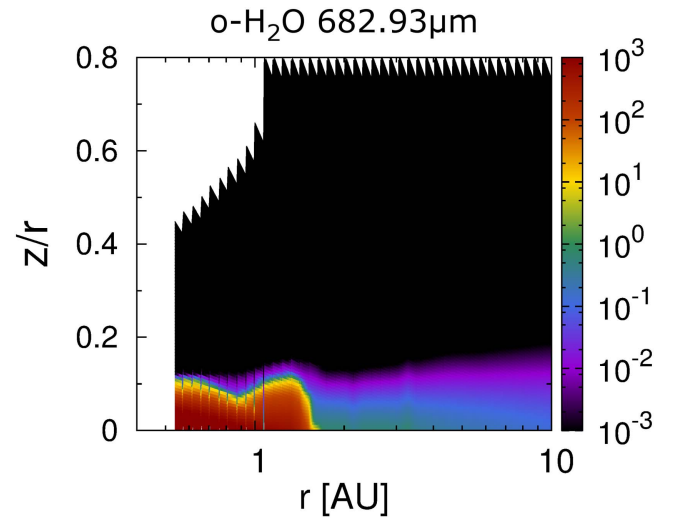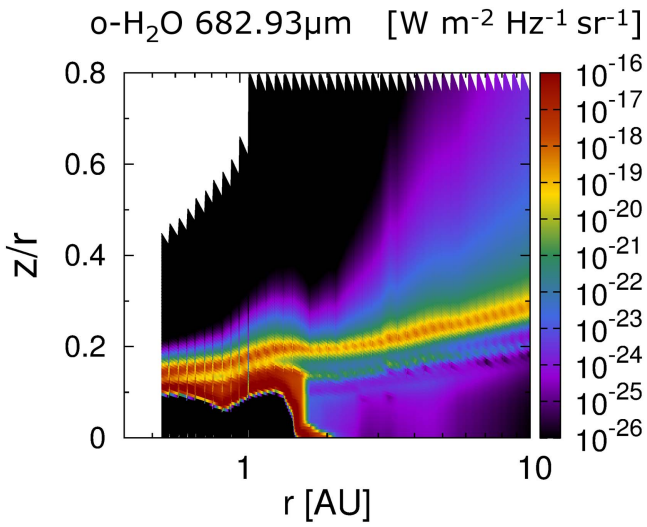
Figure 5. Line-of-sight emissivity distributions of the three characteristic pure rotational ortho-H$_2$O lines with $\lambda = 682.93$ μm (top), 63.37 μm (middle), and 538.66 μm (bottom). The dimension is W m^{-2} Hz^{-1} sr^{-1}. We assume that the inclination angle of the disk i is 0° in making these figures, and thus the direction of line of sight is from $z = +\infty$ to $-\infty$ at each disk radius.

Figure 6. Line-of-sight optical depth $\tau_{ul}(s, x, y, \nu)$ distributions of three characteristic pure rotational ortho-H$_2$O lines at $\lambda = 682.93$ μm (top), 63.37 μm (middle), and 538.66 μm (bottom). We assume that the inclination angle of the disk i is 0° in making these figures, and thus the direction of line of sight is from $z = +\infty$ to $-\infty$ at each disk radius.

Riviere-Marichalar et al. 2012). In addition, the total integrated line flux of classical T Tauri objects in the Taurus molecular cloud are observed to be $\sim 6 \times 10^{-18}$–3×10^{-16} W m^{-2} (e.g., Riviere-Marichalar et al. 2012). These values have a dispersion factor of 50. Riviere-Marichalar et al. (2012) suggested that the objects with higher values of line flux have extended emission from outflows, in contrast to those with lower values that have no extended emissions (e.g., AA Tau, DL Tau, and RY Tau). The latter lower values are of the same order as the value we calculate here assuming a T Tauri disk model with no outflow and envelope.

3.2.3. The Case of a H₂O Emission Line That Traces the Cold Water

In the top right panel of Figure 4, where we show the line profile for the H_2O 538.66 μm line, the contribution from the outer disk (black dashed line, 2–30 au, "out" component) is large compared with that of the optically thick region near the midplane of the inner disk (red solid line, 0–2 au, "in" component) and the shape of the profile is a much narrower double-peaked profile (closer to a single peaked profile), though the A_{ul} is not so high ($=3.497 \times 10^{-3}\,\mathrm{s}^{-1}$). This is because this H_2O 538.66 μm line is the ground-state rotational transition and has low E_{up} ($=61.0$ K) compared with the other lines. The flux of this line comes mainly from the outer cold water reservoir in the photodesorbed layer (see also Section 3.1). We propose that this line is not optimal to detect emission from the innermost water reservoir within the H_2O snowline for the same reasons explained in Section 3.2.2 for the 63.37 μm line (see also the bottom right panel of Figure 4).

According to the bottom panels of Figures 5 and 6, the value of the emissivity at each (r, z) point in the photodesorbed layer is comparable to that of the optically thick region inside the H_2O snowline. The larger surface area of the outer disk, however, means that most disk-integrated emission arises from this region. In addition, the outer disk midplane opacity of this line is larger than that of the H_2O 682.93 μm line, although the wavelength and thus the dust opacity is similar. This is because the abundance of cold H_2O is relatively high, and because this line has low E_{up}.

We mention that previous space high-dispersion spectroscopic observations with *Herschel*/HIFI detected the profiles of this line from disks around one Herbig Ae star (HD 100546) and TW Hya (e.g., Hogerheijde et al. 2011; van Dishoeck et al. 2014). The number of detections is small since the line flux is low compared with the sensitivity of that instrument (Antonellini et al. 2015). The detected line profiles and other line modeling work (e.g., Meijerink et al. 2008; Woitke et al. 2009b; Antonellini et al. 2015; Du et al. 2015) suggested that the emitting region arises in the cold outer disk, consistent with the results of our model calculations. In addition, the total integrated line flux of TW Hya is observed to be $(1.7 \pm 1.1) \times 10^{-19}$ W m^{-2} (Hogerheijde et al. 2011; Du et al. 2015). Considering the difference in distance between TW Hya (~ 51 pc, e.g., Zhang et al. 2013; Du et al. 2015) and our assumed value, 140 pc, the observed flux is within about a factor ≈ 2 of our estimated value (see also Table 1).

We note that previous observations suggested that the OPR of the emitting region is 0.77 for TW Hya (Hogerheijde et al. 2011) derived using the observed para-H_2O ground state 1_{11}–0_{00} 269.47 μm line ($A_{ul} = 1.86 \times 10^{-2}$ and $E_{up} = 53.4$ K) and the observed ortho-H_2O ground state 538.66 μm line. Since we define OPR as three (equal to the value in the high
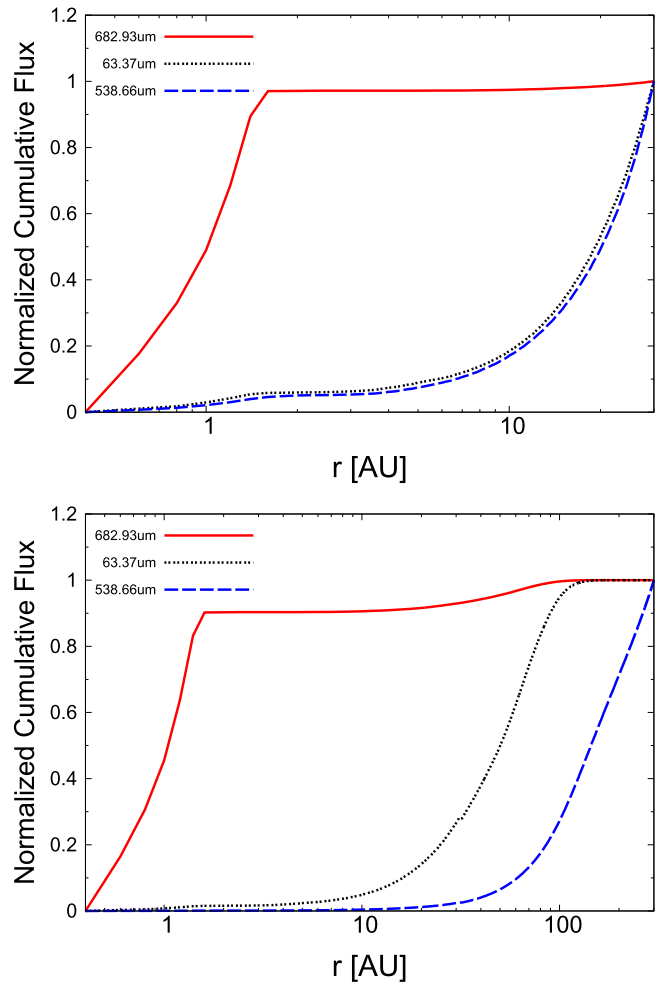
Figure 7. Radial distributions of the normalized cumulative flux for three pure rotational ortho-H_2O lines at $\lambda = 682.93$ μm (red solid line), 63.37 μm (black dotted line), and 538.66 μm (blue dashed line). We normalized the cumulative flux of each line using the values at $r = 30$ au (top panel) and at $r = 300$ au (bottom panel). We assume that the inclination angle of the disk i is 0° in making these figures.

temperature region) throughout the disk (see also Section 2.3), we likely overestimate the line flux of the ortho-H_2O 538.66 μm line. In addition, since the flux of this line is controlled by the outer cold H_2O gas which is desorbed from the cold dust-grain surfaces, it is necessary to include grain-surface reactions (e.g., Hasegawa et al. 1992) to calculate the H_2O gas and ice abundance to more accurately model this region.

3.2.4. Influence of Model Assumptions

Figure 7 shows the radial distributions of normalized cumulative fluxes for these three pure rotational ortho-H_2O lines. We normalized the values of cumulative fluxes of these lines using the values at $r = 30$ au (top panel) and at $r = 300$ au (bottom panel). According to these panels, the 682.93 μm line is emitted mostly from the region inside the H_2O snowline. In contrast, the 63.37 μm line and the 538.66 μm line are emitted mostly from the region outside the H_2O snowline. In addition, although the 63.37 μm line is mainly emitted from the region between $r \sim 10$–100 au, the 538.66 μm line is mainly emitted from a region much further out ($r \sim 50$–300 au). This is because the 682.93 μm line has a

small A_{ul} and a relatively high E_{up}, and thus it mainly emits from the hot H_2O gas inside the H_2O snowline. In contrast, the 63.37 μm line has a large A_{ul}, though E_{up} is similar to that of the 682.93 μm line, and thus the flux density from the hot surface layer of the outer disk is strong (see also Sections 3.1 and 3.2.2). Moreover, the flux density of the 538.66 μm line from the outer cold water reservoir in the photodesorbed layer is strong, since this line is the ground-state rotational transition and has low E_{up} compared with the other lines (see also Sections 3.1 and 3.2.3). These results suggest that the total fluxes of the 538.66 μm line (and partly the 63.37 μm line) will be influenced by the size of the disk, which is included in the calculation of the line profiles, although the 682.93 μm line does not have this problem because the line emitting region is sufficiently small.

Although we adopt a dust-grain size distribution with a maximum radius of $a_{max} \sim 10\,\mu$m throughout the disk (see Appendix A), dust grains are expected to grow in size due to settling and coagulation as the disk evolves and planet formation proceeds. Aikawa & Nomura (2006) calculated disk physical structures with various dust-grain size distributions. In addition, Vasyunin et al. (2011) and Akimkin et al. (2013) calculated the chemical structure of the outer disk ($\gtrsim 10$ au) with grain evolution and discuss its features. They showed that the dust-grain settling and growth reduce the total dust-grain-surface area and lead to higher UV irradiation rates in the upper disk. Therefore, the hot surface layer of the outer disk, which contains abundant gas-phase molecules, including H_2O, gets wider and shifts closer to the disk midplane, thus the abundances and column densities of species are enhanced. However, they did not discuss the midplane structure of the inner disk including the position of the H_2O snowline, since they restricted their calculations to the outer disk ($\gtrsim 10$ au). Here, we note that the position of the H_2O snowline in such an evolved disk is expected to be closer to the central star, since the total dust-grain-surface area and thus dust opacity decreases as the size of dust grains becomes large, leading to a decrease in dust-grain and gas temperatures in the midplane of the inner disk (Oka et al. 2011). Moreover, Ros & Johansen (2013), Zhang et al. (2015), and Banzatti et al. (2015) discussed the effects of rapid dust-grain growth that leads to pebble-sized particles near the H_2O snowline.

As we explained in Section 2.1, the dominant dust heating source in the disk midplane of the inner disk is the radiative flux produced by viscous dissipation (α-disk model), which determines the dust and gas temperature of the region. Recent studies (e.g., Davis 2005; Garaud & Lin 2007; Min et al. 2011; Oka et al. 2011; Harsono et al. 2015; Piso et al. 2015) calculated the evolution of the position of the H_2O snowline in optically thick disks, and showed that it migrates as the disk evolves and as the mass accretion rate in the disk decreases, since the radiative flux produced by viscous dissipation becomes larger as the mass accretion rate increases. We suggest that younger protoplanetary disks like HL Tau (ALMA Partnership et al. 2015) are expected to have a larger mass accretion rate compared with that of our reference T Tauri disk model, and the position of the H_2O snowline will reside further out in the disk midplane. Zhang et al. (2015) argue that the center of the prominent innermost gap at 13 au is coincident with the expected midplane condensation front of water ice. Here we note that Banzatti et al. (2015) and Okuzumi et al. (2016) report the position of the H_2O snowline in HL Tau as

$\lesssim 10$ au. The difference occurs because the midplane radial temperature profile of Zhang et al. (2015) is larger than those of Banzatti et al. (2015) and Okuzumi et al. (2016).

As we described in Section 2.2 and Appendix B, we adopt the wavelength-integrated UV flux calculated at each point by Equations (1) and (2) to approximate the photoreaction rates $k^{ph}(r, z)$ and photodesorption rate k_i^{pd}. This UV flux is estimated by summing up the fluxes of three components: photospheric blackbody radiation, optically thin hydrogenic bremsstrahlung radiation, and strong Lyα line (see also Appendix A). Walsh et al. (2012) pointed out that using Equations (1) and (2), we may overestimate the strength of the UV field at wavelengths other than the Lyα ($\sim$1216 Å). On the basis of their calculations, if we adopt the wavelength dependent UV flux to calculate photochemical reaction rates, the fractional abundance of H_2O vapor in the outer disk surface becomes larger because of the combination of increased gas-phase production and decreased photodestruction. In contrast, the fractional abundance of H_2O vapor in the inner disk midplane is not expected to change, since the UV flux plays a minor role in determining physical and chemical structures around the H_2O snowline (see Figure 1). Walsh et al. (2012) suggested that the column density of H_2O vapor in the outer disk can be enhanced by an order of magnitude depending on the method used to calculate the photodissociation rates.

In the remaining part of this subsection, we discuss the behavior of the H_2O lines for some cases in which we artificially change the distribution of H_2O vapor, the position of the H_2O snowline and the fractional abundance of H_2O gas in the outer disk surface, and test the validity of our model predictions. We explore different values of the H_2O snowline radius to simulate the effects of viscous heating and of different dust opacities due to dust evolution, and of the water abundance to simulate the effects of the strength of photoreactions, as outlined above.

In Figure 8, we show the distributions of H_2O gas and profiles of the 682.93, 63.37, and 538.66 μm lines when we change the positions of the H_2O snowline ($r_{snowline}$) to 1 au (top panels), 4 au (middle panels), 8 au (bottom panels) by hand. In the case of $r_{snowline} = 1$ au, we change the fractional abundance of H_2O gas by hand to 10^{-12} in the regions of $r = 1$–1.6 au and $z/r \sim 0$–1.5. In the cases of $r_{snowline} = 4$ and 8 au, we change the fractional abundance to 5×10^{-5} in the regions of $r = 1.6$–4 au and $z/r \sim 0$–1.5, and $r = 1.6$–8 au and $z/r \sim 0$–1.7, respectively. In calculating these line profiles, we assume that the distance to the object d is 140 pc (approximately the distance of the Taurus molecular cloud), and the inclination angle of the disk i is 30°. Here we note that the disk physical structure is the same as the original reference model (see Figure 1). As the position of the H_2O snowline moves outward, the flux of these three lines from the inner disk becomes larger, that from the outer disk becomes weaker, and the line width, especially the width between the two peaks becomes narrower. In the case of the 682.93 μm line, the emission flux inside the H_2O snowline is still larger than that outside the H_2O snowline, even when the H_2O snowline is artificially set at 1 au. In addition, the position of the H_2O snowline can be distinguished using the difference in the peak separations, although the sensitivity to its position will depend on the spectral resolution of the observations and the uncertainty of other parameters (e.g., inclination i). In the cases of the 63.37 and 538.66 μm lines, the emission fluxes
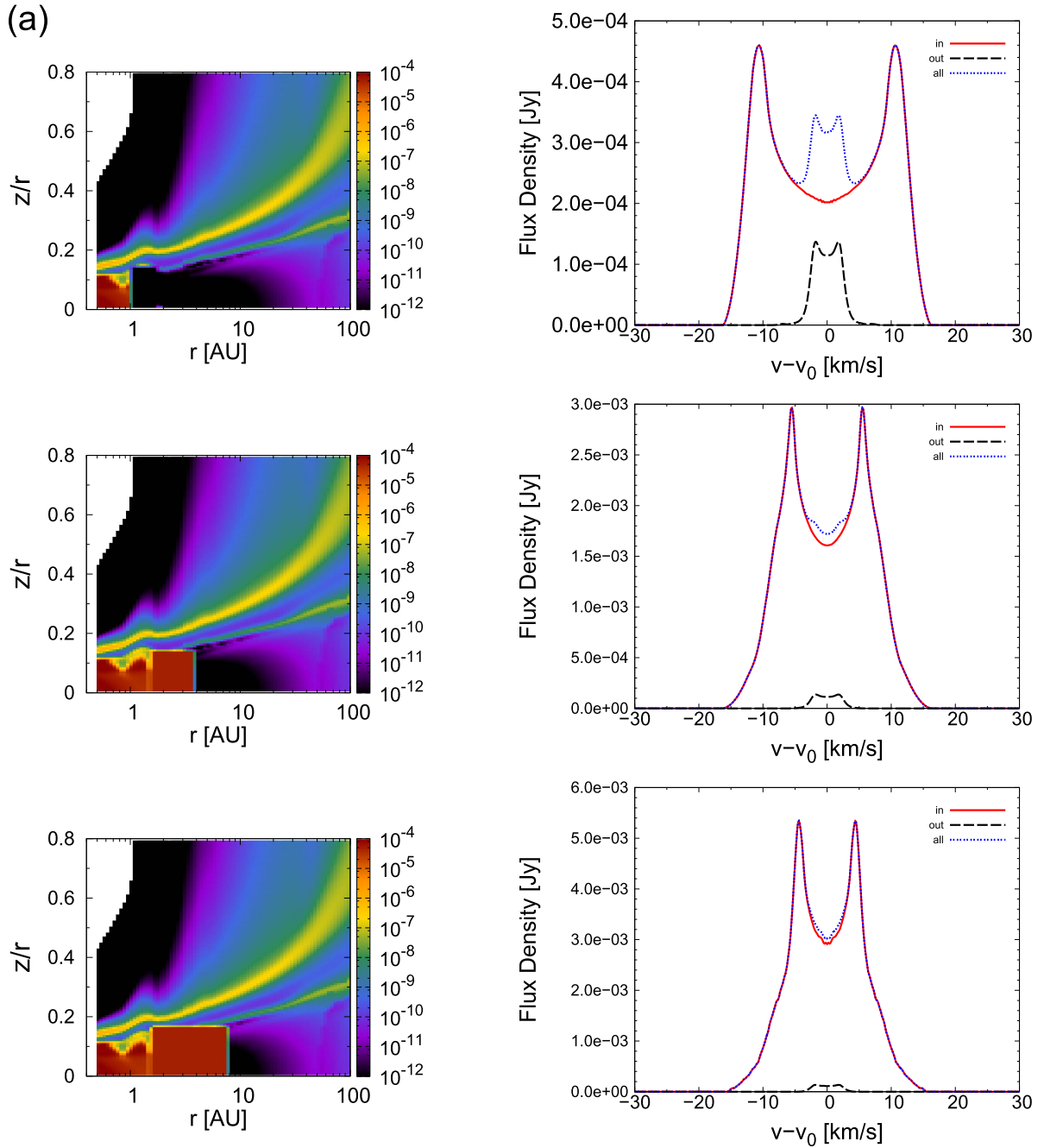
Figure 8. (a) The left three panels: fractional abundance (relative to total hydrogen nuclei density) distributions of H_2O gas of a disk around a T Tauri star as a function of disk radius and height (scaled by the radius, z/r) up to maximum radii of $r = 100$ au. We change the positions of the H_2O snowline to 1 au (top left), 4 au (middle left), 8 au (bottom left) by hand, in order to test the sensitivity to the position of the H_2O snowline. (a) The right three panels: velocity profiles of the pure rotational ortho-H_2O lines at $\lambda = 682.93$ μm ($J_{K_aK_c} = 6_{43}-5_{50}$). The three panels correspond to the cases that the H_2O snowline is assumed to be 1 au (top right) 4 au (middle right), 8 au (bottom right). Red solid lines are the emission line profiles from inside 1, 4, 8 au (approximately inside the H_2O snowline), black dashed lines are those from 1–30, 4–30, 8–30 au (approximately outside the H_2O snowline), and blue dotted lines are those from the total area inside 30 au, respectively. In calculating these profiles, we assume that the distance to the object d is 140 pc (approximately the distance of the Taurus molecular cloud), and the inclination angle of the disk i is 30°. (b) The left three panels: velocity profiles of the pure rotational ortho-H_2O lines at $\lambda = 63.37$ μm ($J_{K_aK_c} = 8_{18}-7_{07}$). (b) The right three panels: velocity profiles of the pure rotational ortho-H_2O lines at $\lambda = 538.66$ μm ($J_{K_aK_c} = 1_{10}-1_{01}$). These panels correspond to the cases that the H_2O snowline is assumed to be 1 au (top left and right), 4 au (middle left and right), 8 au (bottom left and right).

inside the H_2O snowline are still much smaller than that outside the H_2O snowline, even when the H_2O snowline is at 8 au. However, if we calculate the line fluxes using self-consistent physical models, the emission flux of the 63.37 μm line inside the H_2O snowline is around 10 times larger in the case of $r_{snowline} = 8$ au, and its emission flux could be similar to that outside the H_2O snowline (see below).

We use the same disk physical structure as the original reference model, because calculating several different disk physical structures and chemical structures self-consistently using our method (see Sections 2.1 and 2.2) is computationally demanding and beyond the scope of this work. Even if we adopt self-consistent models, we expect that the line widths will not be affected; however, we do expect that the
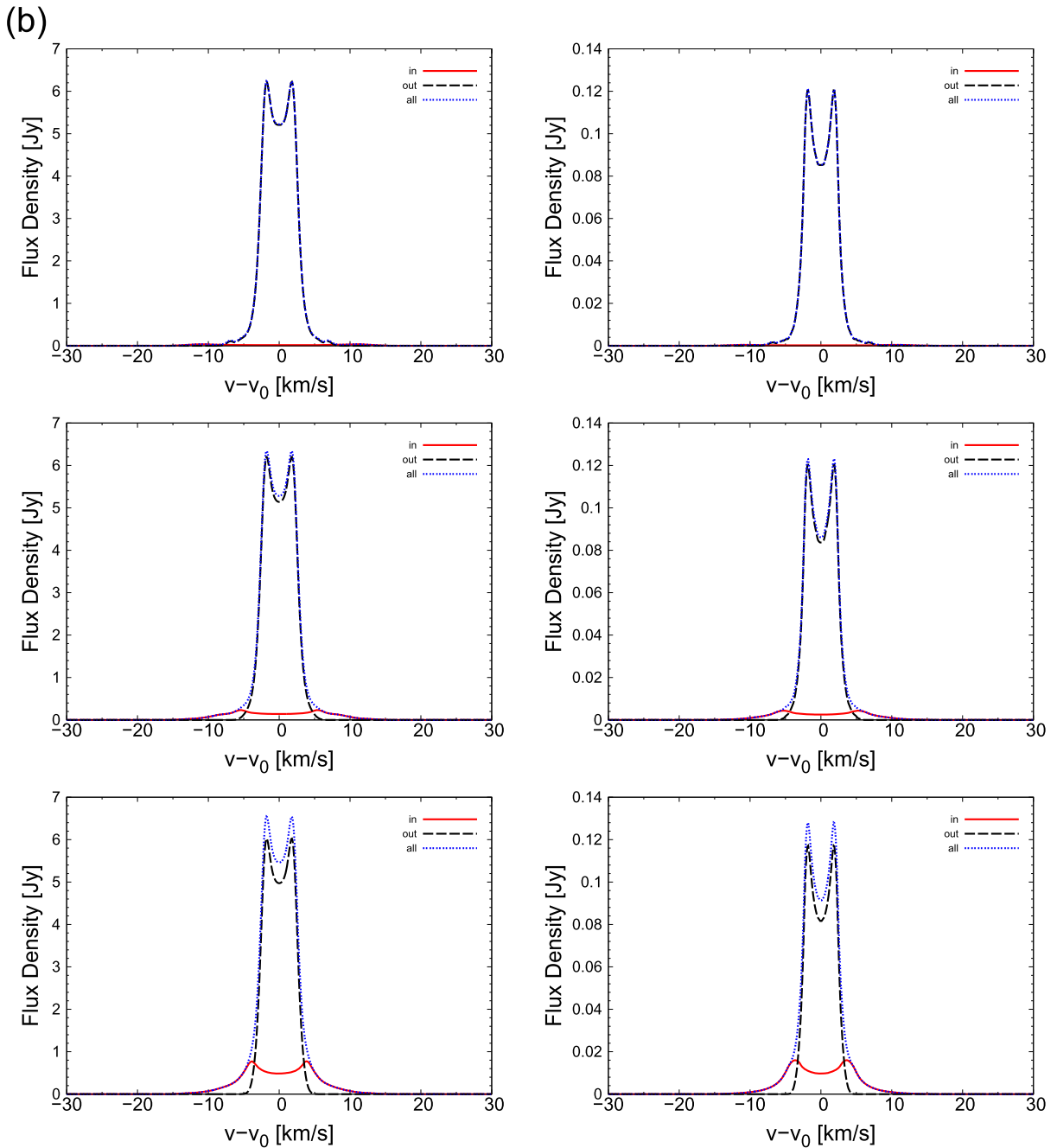
(b)

Figure 8. (Continued.)

line fluxes will be affected since the temperature of line emitting regions will be different. In our original reference model, the gas and dust temperatures around the H_2O snowline are about 150–160 K. In contrast, the temperatures of the line emitting regions around the H_2O snowline for the models with a snowline radius ($r_{snowline}$) of 1 au, 4 au, and 8 au are 180–300 K, 85–90 K, and ∼65 K, respectively. Therefore, estimation of blackbody intensities at $\lambda \sim 63$–$683\,\mu m$ suggests that the line peak flux densities could be ∼0.3–0.85 times lower for the model with $r_{snowline} = 1$ au, and ∼2–4 times and ∼2.5–10 times higher for the models with $r_{snowline} = 4$ au and 8 au, respectively, if we calculate the line fluxes using self-consistent physical models.

These differences in the peak flux densities are larger in the lines at shorter wavelengths.

In Figure 9, we show the distributions of H_2O gas and profiles of the 682.93, 63.37, and $538.66\,\mu m$ lines when we change the fractional abundance of H_2O gas by hand in the hot disk surface of the outer disk to a larger value (10^{-5}, top panels), and to a smaller value (10^{-8}, bottom panels) compared to the original self-consistently calculated value (see also Figure 2), to test the sensitivity of the predictions to the disk surface abundance. If the fractional abundance of H_2O gas in the hot disk surface of the outer disk is larger, the flux of the $682.93\,\mu m$ line from the outer disk becomes larger. Here we note that since the peak velocities of the "in" and "out"
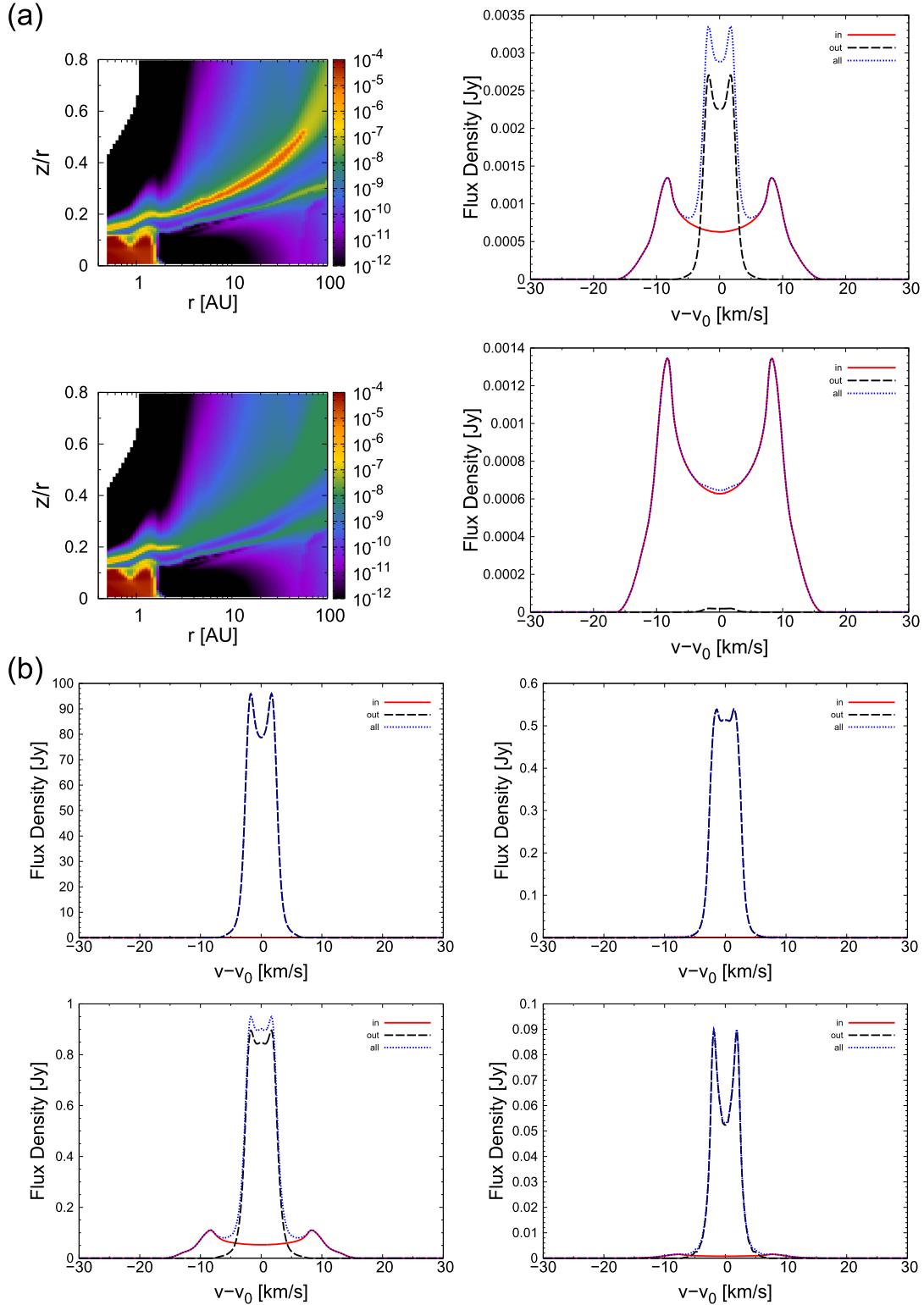
Figure 9. (a) The left two panels: fractional abundance (relative to total hydrogen nuclei density) distributions of H_2O gas of a disk around a T Tauri star as a function of disk radius and height (scaled by the radius, z/r) up to maximum radii of $r = 100$ au. We change the fractional abundance of H_2O gas in the hot disk surface of the outer disk to a larger value (10^{-5}, top left), and to a smaller value (10^{-8}, bottom left) compared with the original self-consistently calculated value (see also Figure 2). (a) The right two panels: velocity profiles of the pure rotational ortho-H_2O lines at $\lambda = 682.93$ μm ($J_{K_aK_c} = 6_{43}-5_{50}$). The two panels correspond to the case of the larger value (10^{-5}, top right), and to the case of the smaller value (10^{-8}, bottom right). Red solid lines are the emission line profiles from inside 2 au ($\sim$inside the H_2O snowline), black dashed lines are those from 2 au to 30 au (approximately outside the H_2O snowline), and blue dotted lines are those from the total area inside 30 au, respectively. In calculating these profiles, we assume that the distance to the object d is 140 pc (approximately the distance of the Taurus molecular cloud), and the inclination angle of the disk i is 30°. (b) The left two panels: velocity profiles of the pure rotational ortho-H_2O lines at $\lambda = 63.37$ μm ($J_{K_aK_c} = 8_{18}-7_{07}$). (b) The right two panels: velocity profiles of the pure rotational ortho-H_2O lines at $\lambda = 538.66$ μm ($J_{K_aK_c} = 1_{10}-1_{01}$). These panels correspond to the case of the larger value (10^{-5}, top left and right), and to the case of the smaller value (10^{-8}, bottom left and right).

components are different, we can separate both components with very high-sensitivity and high-dispersion spectroscopic observations, especially in the very high abundance case (top panels), although the wings of both components are blended. As the abundance in the hot surface of the outer disk becomes small, the fluxes of the 63.37 and 538.66 μm lines from the outer disk become smaller. This effect is stronger in the case of the 63.37 μm line, since this line has a large Einstein A coefficient and high upper state energy compared to those of the 538.66 μm line. However, the contributions of the fluxes of these two lines from the outer disk are still larger than that from the inner disk even when the abundance in the hot surface of the outer disk is small.

3.2.5. Critical Density and the Assumption of LTE

As described in Section 2.3, the level populations of the water molecule (n_u and n_l) are calculated under the assumption of LTE. In this subsection, we discuss the validity of the assumption of LTE within our work.

We calculate the critical density $n_{cr} = A_{ul} \langle \sigma v \rangle^{-1}$ of the three characteristic lines discussed here (ortho-H_2O 682.93, 63.37, 538.66 μm lines, see Table 1). $\langle \sigma v \rangle$ is the collisional rate for the excitation of H_2O by H_2 and electrons for an adopted collisional temperature of 200 K from Faure & Josselin (2008). The critical densities n_{cr} of these three lines are 1.0×10^6, 1.5×10^{10}, and $2.9 \times 10^7 \, cm^{-3}$, respectively. LTE is only realized when collisions dominate the molecular excitation/deexcitation, that is, when the total gas density is larger than n_{cr}. In contrast, non-LTE allows for the fact that the levels may be sub-thermally excited, when n_{cr} is higher than the total gas density, or when the emission (deexcitation) dominates collisions, as well as when the levels are super-thermally excited when the radiative excitation dominates the collisions. When a level is sub-thermally populated in a particular region of the disk, it has a smaller population than in LTE, thus the line flux in non-LTE is smaller than that for LTE (e.g., Meijerink et al. 2009; Woitke et al. 2009b). According to Meijerink et al. (2009), lines with small A_{ul} ($<10^{-2} \, s^{-1}$) and low E_{up} (<2000 K at $r = 1$ au) are close to LTE, since collisions dominate the radiative excitation/deexcitation in those lines.

As described in Section 2.1 (see also Figure 1), the total gas density decreases as a function of disk radius and disk height. We found that the densest region of the disk is in the hot disk midplane inside the H_2O snowline ($\sim 10^{12}$–$10^{14} \, cm^{-3}$), where n_{cr} of the three characteristic lines are much smaller than the total gas density. In contrast, the total gas density in the hot surface layer of the outer disk is $\sim 10^7$–$10^8 \, cm^{-3}$, and that in the photodesorbed layer of water molecules is $\sim 10^8$–$10^{10} \, cm^{-3}$. Therefore, in these regions, the critical densities of the 63.37 and 538.66 μm lines are similar to and larger than the values of the total gas density, while that of the 682.93 μm line is smaller. In Section 3.2.1, we showed that the emission flux of the 682.93 μm line, which traces the H_2O snowline, mainly comes from the hot disk midplane inside the H_2O snowline. Since the value of n_{cr} for this line is much smaller than the total gas density in the line emitting region, it is valid to use the LTE for this region.

On the other hand, in our LTE calculations it remains possible that we have overestimated the emission flux of strong H_2O lines with large A_{ul} that trace the hot surface layer of the outer disk (e.g., the H_2O 63.37 μm line) and lines that trace

cold water vapor in the photodesorbed layer (e.g., the H_2O 538.66 μm line). Previous works, which model such H_2O lines (e.g., Meijerink et al. 2009; Woitke et al. 2009b; Banzatti et al. 2012; Antonellini et al. 2015, 2016), showed that non-LTE calculations are important for these lines. They suggest that non-LTE effects may, however, alter line fluxes by factors of only a few for moderate excitation lines. Moreover, current non-LTE calculations are likely to be inaccurate due to the incompleteness and uncertainty of collisional rates (e.g., Meijerink et al. 2009; Banzatti et al. 2012; Kamp et al. 2013; Zhang et al. 2013; Antonellini et al. 2015).

3.2.6. Requirement for the Observations

Since the velocity width between the emission peaks is ~ 20 km s^{-1}, high-dispersion spectroscopic observations ($R = \lambda/\delta\lambda >$ tens of thousands) of the identified H_2O lines are needed to trace emission from the hot water reservoir within the H_2O snowline. Their profiles potentially contain information that can be used to determine the H_2O snowline position. Moreover, the lines that are suitable to trace emission from the hot water gas within the H_2O snowline (e.g., 682.93 μm) tend to have a much smaller A_{ul} than those detected by previous observations (e.g., 63.37, 538.66 μm). Since the area of the emitting regions are small (radii < 2 au for a T Tauri disk) compared with the total disk size, the total flux of each line is very small (3.12×10^{-22} W m^{-2} for the 682.93 μm line). In addition, the sensitivity and spectral resolution (of some instruments) used for previous mid-infrared, far-infrared, and sub-millimeter observations (e.g., *Spitzer*/IRS, *Herschel*/PACS, *Herschel*/HIFI) were not sufficient to detect and resolve weak lines.

Among the various H_2O lines in ALMA band 8, the H_2O 682.93 μm line is the most suitable to trace emission from the hot water reservoir within the H_2O snowline. Several suitable sub-millimeter H_2O lines exist in ALMA bands 7, 9, and 10 (~ 300–$1000 \, \mu$m), some of which have the same order-of-magnitude fluxes compared with that of the 682.93 μm line. With ALMA, we can now conduct high-sensitivity ($\sim 10^{-21}$–10^{-20} W m^{-2} (5σ, 1 hr)), high-dispersion ($R > 100,000$), and even high spatial resolution (<100 mas) spectroscopic observations. Since the total fluxes of the candidate sub-millimeter lines to trace emission from the hot water reservoir within the H_2O snowline are small in T Tauri disks, they are challenging to detect with current ALMA sensitivity. However, in hotter Herbig Ae disks and in younger T Tauri disks (e.g., HL Tau), the H_2O snowline exists at a larger radius and the flux of these lines will be stronger compared with those in our fiducial T Tauri disk (~ 1.6 au). Thus the possibility of a successful detection is expected to increase in these sources and could be achieved with current ALMA capabilities.

In addition, suitable lines for detection exist over a wide wavelength range, from mid-infrared (Q band) to sub-millimeter, and there are future mid-infrared instruments including the Q band that will enable high-sensitivity and high-dispersion spectroscopic observations: the Mid-Infrared Camera High-disperser and the IFU spectrograph on the Thirty Meter Telescope (TMT/MICHI, e.g., Packham et al. 2012), and HRS of the SPICA[11] Mid-Infrared Instrument (SPICA/SMI). Moreover, since SPICA/SMI has an especially high-sensitivity, successful detection is expected even for a T Tauri

---

[11] http://www.ir.isas.jaxa.jp/SPICA/SPICA_HP/research-en.html

disk with several hours of observation. In our companion paper (Paper II, S. Notsu et al. 2016, in preparation), we will discuss in detail the difference in flux between T Tauri and Herbig Ae disks in lines ranging from the mid-infrared to sub-millimeter wavelengths, and their possible detection with future instruments (e.g., ALMA, TMT/MICHI, SPICA/SMI-HRS).

4. CONCLUSION

In this paper, we identify candidate H_2O lines to trace emission from the hot water reservoir within the H_2O snowline through high-dispersion spectroscopic observations in the near future. First, we calculated the chemical composition of a protoplanetary disk using a self-consistent physical model of a T Tauri disk, and investigated the abundance distributions of H_2O gas and ice. We found that the abundance of H_2O is high ($\sim 10^{-4}$) in the hot inner region within the H_2O snowline (~ 1.6 au) near the equatorial plane, and relatively high $\sim 10^{-7}$ in the hot surface layer of the outer disk, compared to its value in the regions outside the H_2O snowline near the equatorial plane ($\sim 10^{-12}$). Second, we calculated the velocity profiles of H_2O emission lines, and showed that lines (e.g., the ortho-H_2O 682.93 μm line) with small Einstein A coefficients ($A_{ul} \sim 10^{-3}$–10^{-6} s^{-1}) and relatively high upper state energies ($E_{up} \sim 1000$ K) are dominated by emission from the disk region inside the H_2O snowline, and therefore their profiles potentially contain information which can be used to determine the H_2O snowline position. This is because the water gas column density of the region inside the H_2O snowline is sufficiently high that all lines emitting from this region are optically thick as long as $A_{ul} > 10^{-6}$ s^{-1}. Instead, the region outside the H_2O snowline has a lower water gas column density and lines with larger Einstein A coefficients have a more significant contribution to their fluxes since the lines are expected to be optically thin there. Therefore, we argue that the H_2O lines with small Einstein A coefficients and relatively high upper state energies are the most suitable to trace emission from the hot water reservoir within the H_2O snowline in disks through high-dispersion spectroscopic observations in the near future. The wavelengths of those lines suitable to trace emission from the hot water reservoir within the H_2O snowline range from mid-infrared (Q band) to sub-millimeter, and they overlap with the capabilities of ALMA and future mid-infrared high-dispersion spectrographs (e.g., TMT/MICHI, SPICA/ SMI-HRS). In addition, we calculate the behavior of water lines that have been detected by previous spectroscopic observations (e.g., the ortho-H_2O 63.37 μm line, the ortho-H_2O 538.66 μm line). The fluxes calculated for these lines are consistent with those of previous observations and models. These lines are less suited to trace emission from water vapor within the H_2O snowline because they are mainly emitted from the region outside the snowline. In a future paper (Paper II, S. Notsu et al. 2016, in preparation), we will discuss the differences of fluxes in the suitable lines ranging from mid-infrared (Q band) to sub-millimeter, and the possibility of future observations (e.g., ALMA, TMT/MICHI, SPICA) to locate the position of the H_2O snowline.

APPENDIX A
THE X-RAY AND UV RADIATION FIELD AND THE DUST-GRAIN MODELS

We adopt the model X-ray spectrum of a T Tauri star created by fitting the observed *XMM-Newton* spectrum of TW Hya (Kastner et al. 2002), the classical T Tauri star, with a two-temperature thin thermal plasma model (MEKAL model; see, e.g., Liedahl et al. 1995). The best-fit parameters are $kT_1 = 0.8$ keV and $kT_2 = 0.2$ for the plasma temperatures and $N_H = 2.7 \times 10^{20}$ cm^{-2} for the foreground interstellar hydrogen column density. This is the same model that is adopted in Nomura et al. (2007).

The stellar UV radiation field model we use is based on the observational data of TW Hya, with a stellar UV radiation field that has three components: photospheric blackbody radiation, optically thin hydrogenic bremsstrahlung radiation, and strong Lyα line emission (for details, see Appendix B of Nomura & Millar 2005, Walsh et al. 2015). For the UV extinction, we include absorption and scattering by dust grains. The interstellar UV radiation field is taken into account, but its contribution is negligible since the UV irradiation of the central star is strong (Nomura & Millar 2005).

We adopt the same dust-grain model of Nomura & Millar (2005). They assume that the dust grains are compact and spherical, and consist of silicate grains, carbonaceous grains, and water ices. The optical properties of the carbonaceous grains are assumed to have a continuous distribution of graphite-like properties for larger sizes and PAH-like properties in the small size limit (Li & Draine 2001). The sublimation temperatures are assumed to be $T_{silicate} = 1500$ K, $T_{carbon} = 2300$ K, and $T_{ice} = 150$ K (Adams & Shu 1986). The mass fractional abundances are taken to be consistent with the solar elemental abundances: $\zeta_{silicate} = 0.0043$, $\zeta_{carbon} = 0.0030$, and $\zeta_{ice} = 0.0094$ (Anders & Grevesse 1989). Their bulk densities are set to be $\rho_{silicate} = 3.5$ g cm^{-3}, $\rho_{graphite} = 2.24$ g cm^{-3}, and $\rho_{ice} = 0.92$ g cm^{-3}. They assume that the dust and gas are well mixed. They use the dust-grain size distributions of silicate and carbonaceous grains obtained by Weingartner & Draine (2001), which reproduces the extinction curve observed in dense clouds with the ratio of visual extinction to reddening $R_V \equiv A(V)/E(B-V) = 5.5$. They adopt the value of $b_C = 3.0 \times 10^{-5}$, which is the total C abundance per H nucleus in the log-normal size dust-grain distribution, in order to reproduce the distribution of very small hydrocarbon molecules including PAHs (see also Figure 6 of Weingartner & Draine 2001). It is assumed that the water ice has the simple size distribution of $dn/da \propto a^{-3.5}$, where a is the radius of the dust particles (Mathis et al. 1977). The maximum radius of dust grains a_{max} is ~ 10 μm. The calculated monochromatic absorption coefficient is shown in Figure D.1. of Nomura & Millar (2005).

APPENDIX B
THE MECHANISMS OF NON-THERMAL DESORPTION

The non-thermal desorption mechanisms we adopt are cosmic-ray-induced desorption (Leger et al. 1985; Hasegawa & Herbst 1993) and photodesorption from UV photons (Westley et al. 1995; Willacy & Langer 2000; Öberg et al. 2007), in common with some previous studies (e.g., Walsh et al. 2010, 2012). In this subsection, we explain the details of these non-thermal desorption mechanisms.

In order to calculate the cosmic-ray-induced desorption rate for each species, k_i^{crd}, we assume that dust grains with a radius of 0.1 μm are impulsively heated by the impact of relativistic Fe nuclei with energies of 20–70 MeV nucleon^{-1} which deposit an energy of 0.4 MeV on average into each dust grain (Leger et al. 1985; Hasegawa & Herbst 1993). Assuming that the majority of molecules desorb around 70 K, the cosmic-ray-induced desorption rate can be approximated by

$$k_i^{\mathrm{crd}} = f(70\,\mathrm{K}) k_i^d(70\,\mathrm{K}) \frac{\zeta_{\mathrm{CR}}}{1.36 \times 10^{-17}\,\mathrm{s}^{-1}}\,\mathrm{s}^{-1}, \qquad (17)$$

where ζ_{CR} is the cosmic-ray ionization rate of H_2, $k_i^d(70\,\mathrm{K})$ is the thermal desorption energy of species i at a dust temperature of 70 K computed using Equation (4). $f(70\,\mathrm{K})$ is the fraction of time spent by dust grains around 70 K and is defined as the ratio of the desorption cooling time (10^{-5} s) to the time interval between successive heatings to 70 K. The latter value is estimated to be 3.16×10^{13} s from the Fe cosmic-ray flux, then $f(70\,\mathrm{K})$ is 3.16×10^{-19} (Leger et al. 1985; Hasegawa & Herbst 1993). We mention that like cosmic-ray particles, X-ray photons can penetrate deep inside the disk and locally heat dust grains. However, X-ray desorption is not yet included in our chemical code unlike previous studies (e.g., Walsh et al. 2012, 2014b, 2015). This is because X-ray desorption is the least theoretically or experimentally constrained of all the non-thermal desorption mechanisms, and thus there remain significant uncertainties in the reaction rates (e.g., Najita et al. 2001; Walsh et al. 2010).

Absorption of a UV photon by a dust-grain surface species can increase the species' internal energy enough to induce desorption. The photodesorption rate of species i is given by

$$k_i^{\mathrm{pd}} = F_{\mathrm{UV}} Y_{\mathrm{UV}}^i \sigma_d \frac{n_d}{n_{\mathrm{act}}}\,\mathrm{s}^{-1}, \qquad (18)$$

where F_{UV} is the wavelength-integrated UV radiative flux calculated at each (r, z) in units of photons cm^{-2} s^{-1}. Y_{UV}^i is the experimentally determined photodesorption yield in units of molecules photon^{-1}. Woitke et al. (2009a) and Heinzeller et al. (2011) used a similar method to calculate k_i^{pd}. F_{UV} is calculated from the density profile and the dust opacity in our adopted disk physical model (Nomura & Millar 2005; Nomura et al. 2007; Walsh et al. 2015). We assume that Y_{UV}^i is 3.0×10^{-3} for all species, which is the same value determined for pure water ice by Westley et al. (1995) and for pure CO ice by Öberg et al. (2007). Walsh et al. (2010) use the same value of Y_{UV}^i. $n_{\mathrm{act}} = 4\pi a^2 n_d n_{\mathrm{surf}} N_{\mathrm{Lay}}$ is the number of active surface sites in the ice mantle per unit volume. N_{Lay} is the number of surface layers to be considered as "active," and we adopt the value of Aikawa et al. (1996), $N_{\mathrm{Lay}} = 2$. Recent experiments by Öberg et al. (2009a, 2009b, 2009c) suggest that photodesorption rates are dependent on ice composition and the depth of the ice layer on a dust grain.

REFERENCES

Adams, F. C., & Shu, F. H. 1986, ApJ, 308, 836
Aikawa, Y., Miyama, S. M., Nakano, T., & Umebayashi, T. 1996, ApJ, 467, 684
Aikawa, Y., & Nomura, H. 2006, ApJ, 642, 1152
Akimkin, V., Zhukovska, S., Wiebe, D., et al. 2013, ApJ, 766, 8
Akiyama, E., Muto, T., Kusakabe, N., et al. 2015, ApJL, 802, L17
ALMA Partnership, Brogan, C. L., Pérez, L. M., et al. 2015, ApJL, 808, L3
Anders, E., & Grevesse, N. 1989, GeCoA, 53, 197
Andrews, S. M., Wilner, D. J., Zhu, Z., et al. 2016, ApJL, 820, L40
Antonellini, S., Kamp, I., Lahuis, F., et al. 2016, A&A, 585, A61
Antonellini, S., Kamp, I., Riviere-Marichalar, P., et al. 2015, A&A, 582, A105
Armitage, P. J. 2011, ARA&A, 49, 195
Banzatti, A., Meyer, M. R., Bruderer, S., et al. 2012, ApJ, 745, 90
Banzatti, A., Pinilla, P., Ricci, L., et al. 2015, ApJL, 815, L15
Barber, R. J., Tennyson, J., Harris, G. J., & Tolchenov, R. N. 2006, MNRAS, 368, 1087
Benisty, M., Juhasz, A., Boccaletti, A., et al. 2015, A&A, 578, L6
Blevins, S. M., Pontoppidan, K. M., Banzatti, A., et al. 2016, ApJ, 818, 22
Brown, W. A., & Bolina, A. S. 2007, MNRAS, 374, 1006
Carr, J. S., & Najita, J. R. 2008, Sci, 319, 1504
Carr, J. S., & Najita, J. R. 2011, ApJ, 733, 102
Caselli, P., & Ceccarelli, C. 2012, A&ARv, 20, 56
Davis, S. S. 2005, ApJ, 620, 994
Dent, W. R. F., Thi, W. F., Kamp, I., et al. 2013, PASP, 125, 477
Dominik, C., Ceccarelli, C., Hollenbach, D., & Kaufman, M. 2005, ApJL, 635, L85
Drozdovskaya, M. N., Walsh, C., Visser, R., Harsono, D., & van Dishoeck, E. F. 2014, MNRAS, 445, 913
Du, F., & Bergin, E. A. 2014, ApJ, 792, 2
Du, F., Bergin, E. A., & Hogerheijde, M. R. 2015, ApJL, 807, L32
Dutrey, A., Semenov, D., Chapillon, E., et al. 2014, Protostars and Planets VI (Tuscon, AZ: Univ. Arizona Press)
Edridge, J. L. 2010, PhD thesis, Univ. College London
Faure, A., & Josselin, E. 2008, A&A, 492, 257
Fedele, D., Bruderer, S., van Dishoeck, E. F., et al. 2012, A&A, 544, LL9
Fedele, D., Bruderer, S., van Dishoeck, E. F., et al. 2013, A&A, 559, AA77
Fedele, D., Pascucci, I., Brittain, S., et al. 2011, ApJ, 732, 106
Fukagawa, M., Tsukagoshi, T., Momose, M., et al. 2013, PASJ, 65, L14
Furuya, K., & Aikawa, Y. 2014, ApJ, 790, 97
Furuya, K., Aikawa, Y., Nomura, H., Hersant, F., & Wakelam, V. 2013, ApJ, 779, 11
Garaud, P., & Lin, D. N. C. 2007, ApJ, 654, 606
Glassgold, A. E., Meijerink, R., & Najita, J. R. 2009, ApJ, 701, 142
Goto, M., Usuda, T., Dullemond, C. P., et al. 2006, ApJ, 652, 758
Graedel, T. E., Langer, W. D., & Frerking, M. A. 1982, ApJS, 48, 321
Hama, T., Kouchi, A., & Watanabe, N. 2016, Sci, 351, 65
Harsono, D., Bruderer, S., & van Dishoeck, E. F. 2015, A&A, 582, A41
Hasegawa, T. I., & Herbst, E. 1993, MNRAS, 261, 83
Hasegawa, T. I., Herbst, E., & Leung, C. M. 1992, ApJS, 82, 167
Hayashi, C. 1981, PThPS, 70, 35
Hayashi, C., Nakazawa, K., & Nakagawa, Y. 1985, Protostars and Planets II (Tuscon, AZ: Univ. Arizona Press)
Heinzeller, D., Nomura, H., Walsh, C., & Millar, T. J. 2011, ApJ, 731, 115
Henning, T., & Semenov, D. 2013, ChRv, 113, 9016
Hogerheijde, M. R., Bergin, E. A., Brinch, C., et al. 2011, Sci, 334, 338
Hogerheijde, M. R., & van der Tak, F. F. S. 2000, A&A, 362, 697
Honda, M., Inoue, A. K., Fukagawa, M., et al. 2009, ApJL, 690, L110
Honda, M., Kudo, T., Takatsuki, S., et al. 2016, ApJ, 821, 2
Inoue, A. K., Honda, M., Nakamoto, T., & Oka, A. 2008, PASJ, 60, 557
Ishimoto, D., Nomura, H., Heinzeller, D., et al. 2013, in New Trends in Radio Astronomy in the ALMA Era: The 30th Anniversary of Nobeyama Radio Observatory, Vol. 476 (San Francisco, CA: ASP), 393
Kamp, I., Thi, W.-F., Meeus, G., et al. 2013, A&A, 559, A24
Kastner, J. H., Huenemoerder, D. P., Schulz, N. S., Canizares, C. R., & Weintraub, D. A. 2002, ApJ, 567, 434
Kenyon, S. J., & Hartmann, L. 1995, ApJS, 101, 117
Leger, A., Jura, M., & Omont, A. 1985, A&A, 144, 147
Li, A., & Draine, B. T. 2001, ApJ, 554, 778
Liedahl, D. A., Osterheld, A. L., & Goldstein, W. H. 1995, ApJL, 438, L115
Mandell, A. M., Bast, J., van Dishoeck, E. F., et al. 2012, ApJ, 747, 92

Martin, R. G., & Livio, M. 2012, MNRAS, 425, L6
Martin, R. G., & Livio, M. 2013, MNRAS, 434, 633
Masuda, K., Takahashi, J., & Mukai, T. 1998, A&A, 330, 773
Mathews, G. S., Klaassen, P. D., Juhász, A., et al. 2013, A&A, 557, A132
Mathis, J. S., Rumpl, W., & Nordsieck, K. H. 1977, ApJ, 217, 425
Matsumura, S., Brasser, R., & Ida, S. 2016, ApJ, 818, 15
McClure, M. K., Espaillat, C., Calvet, N., et al. 2015, ApJ, 799, 162
McClure, M. K., Manoj, P., Calvet, N., et al. 2012, ApJL, 759, LL10
McElroy, D., Walsh, C., Markwick, A. J., et al. 2013, A&A, 550, A36
Meeus, G., Montesinos, B., Mendigutía, I., et al. 2012, A&A, 544, AA78
Meijerink, R., Aresu, G., Kamp, I., et al. 2012, A&A, 547, A68
Meijerink, R., Poelman, D. R., Spaans, M., Tielens, A. G. G. M., & Glassgold, A. E. 2008, ApJL, 689, L57
Meijerink, R., Pontoppidan, K. M., Blake, G. A., Poelman, D. R., & Dullemond, C. P. 2009, ApJ, 704, 1471
Min, M., Dullemond, C. P., Kama, M., & Dominik, C. 2011, Icar, 212, 416
Morbidelli, A., Chambers, J., Lunine, J. I., et al. 2000, M&PS, 35, 1309
Morbidelli, A., Lunine, J. I., O'Brien, D. P., Raymond, S. N., & Walsh, K. J. 2012, AREPS, 40, 251
Mulders, G. D., Ciesla, F. J., Min, M., & Pascucci, I. 2015, ApJ, 807, 9
Mumma, M. J., & Charnley, S. B. 2011, ARA&A, 49, 471
Mumma, M. J., Weaver, H. A., & Larson, H. P. 1987, A&A, 187, 419
Muto, T., Grady, C. A., Hashimoto, J., et al. 2012, ApJL, 748, LL22
Najita, J., Bergin, E. A., & Ullom, J. N. 2001, ApJ, 561, 880
Najita, J. R., Carr, J. S., Pontoppidan, K. M., et al. 2013, ApJ, 766, 134
Nomura, H., Aikawa, Y., Tsujimoto, M., Nakagawa, Y., & Millar, T. J. 2007, ApJ, 661, 334
Nomura, H., & Millar, T. J. 2005, A&A, 438, 923
Nomura, H., Tsukagoshi, T., Kawabe, R., et al. 2016, ApJL, 819, L7
Öberg, K. I., Fuchs, G. W., Awad, Z., et al. 2007, ApJL, 662, L23
Öberg, K. I., Furuya, K., Loomis, R., et al. 2015, ApJ, 810, 112
Öberg, K. I., Garrod, R. T., van Dishoeck, E. F., & Linnartz, H. 2009a, A&A, 504, 891
Öberg, K. I., Linnartz, H., Visser, R., & van Dishoeck, E. F. 2009b, ApJ, 693, 1209
Öberg, K. I., Murray-Clay, R., & Bergin, E. A. 2011, ApJL, 743, L16
Öberg, K. I., van Broekhuizen, F., Fraser, H. J., et al. 2005, ApJL, 621, L33
Öberg, K. I., van Dishoeck, E. F., & Linnartz, H. 2009c, A&A, 496, 281
Oka, A., Nakamoto, T., & Ida, S. 2011, ApJ, 738, 141
Okuzumi, S., Momose, M., Sirono, S.-i., Kobayashi, H., & Tanaka, H. 2016, ApJ, 821, 82
Packham, C., Honda, M., Richter, M., et al. 2012, Proc. SPIE, 8446, 84467G
Piso, A.-M. A., Öberg, K. I., Birnstiel, T., & Murray-Clay, R. A. 2015, ApJ, 815, 109
Pontoppidan, K. M., Blake, G. A., & Smette, A. 2011, ApJ, 733, 84
Pontoppidan, K. M., Blake, G. A., van Dishoeck, E. F., et al. 2008, ApJ, 684, 1323
Pontoppidan, K. M., & Blevins, S. M. 2014, FaDi, 169, 49
Pontoppidan, K. M., Dullemond, C. P., van Dishoeck, E. F., et al. 2005, ApJ, 622, 463
Pontoppidan, K. M., Salyk, C., Bergin, E. A., et al. 2014, Protostars and Planets VI (Tuscon, AZ: Univ. Arizona Press)
Pontoppidan, K. M., Salyk, C., Blake, G. A., et al. 2010a, ApJ, 720, 887
Pontoppidan, K. M., Salyk, C., Blake, G. A., & Käufl, H. U. 2010b, ApJL, 722, L173

Qi, C., Öberg, K. I., Andrews, S. M., et al. 2015, ApJ, 813, 128
Qi, C., Öberg, K. I., & Wilner, D. J. 2013a, ApJ, 765, 34
Qi, C., Öberg, K. I., Wilner, D. J., et al. 2013b, Sci, 341, 630
Rapson, V. A., Kastner, J. H., Millar-Blanchaer, M. A., & Dong, R. 2015, ApJL, 815, L26
Riviere-Marichalar, P., Ménard, F., Thi, W. F., et al. 2012, A&A, 538, LL3
Ros, K., & Johansen, A. 2013, A&A, 552, A137
Rybicki, G. B., & Lightman, A. P. 1986, in Radiative Processes in Astrophysics, ed. G. B. Rybicki & A. P. Lightman, (New York: Wiley-VCH), 400
Salyk, C., Lacy, J. H., Richter, M. J., et al. 2015, ApJL, 810, L24
Salyk, C., Pontoppidan, K. M., Blake, G. A., et al. 2008, ApJL, 676, L49
Salyk, C., Pontoppidan, K. M., Blake, G. A., Najita, J. R., & Carr, J. S. 2011, ApJ, 731, 130
Sandford, S. A., & Allamandola, L. J. 1993, ApJ, 417, 815
Sato, T., Okuzumi, S., & Ida, S. 2016, A&A, 589, A15
Schöier, F. L., van der Tak, F. F. S., van Dishoeck, E. F., & Black, J. H. 2005, A&A, 432, 369
Schwarz, K. R., Bergin, E. A., Cleeves, L. I., et al. 2016, ApJ, 823, 91
Semenov, D., & Wiebe, D. 2011, ApJS, 196, 25
Shakura, N. I., & Sunyaev, R. A. 1973, A&A, 24, 337
Tennyson, J., Zobov., N. F., Williamson, R., Polyansky, O. L., & Bernath, P. F. 2001, JPCRD, 30, 735
Terada, H., Tokunaga, A. T., Kobayashi, N., et al. 2007, ApJ, 667, 303
van der Marel, N., van Dishoeck, E. F., Bruderer, S., et al. 2013, Sci, 340, 1199
van der Marel, N., van Dishoeck, E. F., Bruderer, S., et al. 2016, A&A, 585, A58
van Dishoeck, E. F., Bergin, E. A., Lis, D. C., & Lunine, J. I. 2014, Protostars and Planets VI (Tuscon, AZ: Univ. Arizona Press)
van Dishoeck, E. F., Herbst, E., & Neufeld, D. A. 2013, ChRv, 113, 9043
van Dishoeck, E. F., Jonkheid, B., & van Hemert, M. C. 2006, FaDi, 133, 231
Vasyunin, A. I., Wiebe, D. S., Birnstiel, T., et al. 2011, ApJ, 727, 76
Veeraghattam, V. K., Manrodt, K., Lewis, S. P., & Stancil, P. C. 2014, ApJ, 790, 4
Wada, K., Tanaka, H., Okuzumi, S., et al. 2013, A&A, 559, AA62
Walsh, C., Harada, N., Herbst, E., & Millar, T. J. 2009, ApJ, 700, 752
Walsh, C., Juhász, A., Pinilla, P., et al. 2014a, ApJL, 791, L6
Walsh, C., Millar, T. J., & Nomura, H. 2010, ApJ, 722, 1607
Walsh, C., Millar, T. J., Nomura, H., et al. 2014b, A&A, 563, AA33
Walsh, C., Nomura, H., Millar, T. J., & Aikawa, Y. 2012, ApJ, 747, 114
Walsh, C., Nomura, H., & van Dishoeck, E. 2015, A&A, 582, A88
Weingartner, J. C., & Draine, B. T. 2001, ApJ, 548, 296
Westley, M. S., Baragiola, R. A., Johnson, R. E., & Baratta, G. A. 1995, Natur, 373, 405
Willacy, K. 2007, ApJ, 660, 441
Willacy, K., & Langer, W. D. 2000, ApJ, 544, 903
Woitke, P., Kamp, I., & Thi, W.-F. 2009a, A&A, 501, 383
Woitke, P., Thi, W.-F., Kamp, I., & Hogerheijde, M. R. 2009b, A&A, 501, L5
Woodall, J., Agúndez, M., Markwick-Kemper, A. J., & Millar, T. J. 2007, A&A, 466, 1197
Yamamoto, T., Nakagawa, N., & Fukui, Y. 1983, A&A, 122, 171
Zhang, K., Blake, G. A., & Bergin, E. A. 2015, ApJL, 806, L7
Zhang, K., Pontoppidan, K. M., Salyk, C., & Blake, G. A. 2013, ApJ, 766, 82